

This is a non-peer reviewed preprint submitted to EarthArXiv

**Controls on Mg isotopic fractionation between deep
mantle phases and relict signatures of a terrestrial
magma ocean**

A. M. Walker, Remco C. Hin and Tim Elliott

Addresses: Department of Earth Sciences, University of Oxford, South Parks Road, Oxford, OX1 3AN, UK,
Institute of Environmental Geology and Geoengineering, Consiglio Nazionale delle Ricerche, Via Mario Bianco 9,
20131, Milano MI, Italy and School of Earth Sciences, University of Bristol, Wills Memorial Building, Queen's
Road, Bristol, BS8 1RJ, UK. email: andrew.walker@earth.ox.ac.uk

This manuscript is under review at *Geochimica et Cosmochimica Acta*

Controls on Mg isotopic fractionation between deep mantle phases and relict signatures of a terrestrial magma ocean

Andrew M. Walker^{a,*}, Remco C. Hin^b, Tim Elliott^c

^a*Department of Earth Sciences, University of Oxford, South Parks Road, Oxford, OX1 3AN, UK*

^b*Institute of Environmental Geology and Geoengineering, Consiglio Nazionale delle Ricerche, Via Mario Bianco 9, 20131, Milano MI, Italy*

^c*School of Earth Sciences, University of Bristol, Wills Memorial Building, Queen's Road, Bristol, BS8 1RJ, UK*

Abstract

1 We use density functional theory to investigate the fractionation of Mg
2 isotopes between phases in the lower mantle. Our results support previ-
3 ous work and show that coordination number plays an important role in
4 controlling isotopic fractionation, with bridgmanite (perovskite-structured
5 MgSiO₃) preferentially incorporating lighter Mg isotopes into its highly co-
6 ordinated site compared to periclase (MgO). Increasing pressure enhances
7 this fractionation while increasing temperature decreases it. These two ef-
8 fects trade-off such that the preference is evident across all lower mantle
9 conditions explored, even to the high temperatures of the chondritic liquidus
10 (e.g. $\Delta^{26/24}\text{Mg}_{\text{Per-Bdm}}$ is 0.04‰ at 4200 K and 87 GPa). In additional
11 numerical experiments we separate the effect of coordination number from
12 differences in bond length between different phases and these allow us to

*Corresponding author

Email address: andrew.walker@earth.ox.ac.uk (Andrew M. Walker)

13 build an ionic model which parameterises magnesium isotope fractionation
14 as a function of bond length, coordination number, and temperature. This
15 model provides us with a preliminary means to describe isotope partition-
16 ing between solid and liquid phases when making predictions of Mg isotopic
17 differences generated during terrestrial magma ocean crystallisation. We
18 find that Mg isotopic fractionation between bridgmanite and melt, at lower
19 mantle conditions, is sufficient to generate detectable differences in the Mg
20 isotopic compositions of a residual melt or solid cumulate phase, relative to
21 bulk Earth. More specifically, we show that isolation of a reservoir of cumu-
22 late bridgmanite that is some 3-15% by mass of the mantle could account for
23 the super-chondritic $^{26}\text{Mg}/^{24}\text{Mg}$ of accessible terrestrial peridotite samples.
24 Whether such a reservoir can be dynamically preserved over Earth history
25 remains an open question, but our results help quantify possible tests of such
26 a scenario.

Keywords: Mg isotopes, density functional theory, ionic model,
coordination number, magma ocean

27 **1. Introduction**

28 Study of mass-dependent isotopic variations has traditionally been the
29 domain of low temperature geochemists, since the magnitudes of such frac-
30 tionations are inversely proportional to temperature squared (Urey, 1947)
31 and so most evident at the Earth's surface. However, realisation of the op-
32 portunity afforded by multicollector inductively coupled plasma mass spec-
33 trometers to make isotopic measurements of a wide range of elements to
34 precisions significantly better than 100 ppm makes this discipline of increas-

35 ing interest for the study of high-temperature processes (e.g. Young et al.,
36 2015; Soderman et al., 2022; Wang et al., 2023). Although small, isotopic
37 differences generated in the Earth’s interior are now typically amenable to
38 analysis.

39 A likely important factor in the magnitude of mass-dependent isotopic
40 fractionations in the deep Earth is the effect of pressure. Whilst the high
41 temperatures of the planet’s interior act against mass-dependent isotopic
42 variability, associated increases in pressure and the resulting changes in the
43 coordination number and bond length of common mineral sites can act to
44 promote isotopic fractionation. The work of Huang et al. (2013, 2014) and
45 Wu et al. (2015) examined the interplay of these counter-acting continuous
46 and discontinuous changes with depth for the major elements Mg and Si.
47 Here we take some further steps in this direction by making a first princi-
48 ples exploration of the isotopic fractionation of magnesium between mantle
49 phases over a wide range of appropriate pressures and temperatures. In par-
50 ticular, we wish to estimate fractionation factors for key phases, at a range
51 of lower mantle conditions, to assess Mg isotopic fractionations that may be
52 associated with magma ocean crystallisation.

53 Magnesium is an attractive target because it is a high-abundance, stoi-
54 chiometric constituent of several major mantle phases, that occurs in only
55 one oxidation state. There is also a comparatively large (8%) relative mass
56 difference between its two major isotopes, which is an important contributing
57 factor in the generation of discernible isotopic fractionation.

58 Magnesium isotopic differences inferred to result from equilibrium parti-
59 tioning between co-existing, shallow mantle minerals have been reported for

60 more than a decade (e.g. Young et al., 2009). Such observations, supported
61 by theory and modelling (Young et al., 2009; Schauble, 2011; Huang et al.,
62 2013), have led to a useful rule of thumb that the isotopic composition of
63 an element in a more highly coordinate lattice site is lighter than in a site
64 with lower coordination. In this general context, it is significant that high
65 pressure phases hosting Mg show a range of coordination numbers from 6-
66 fold in periclase (Per: rock salt structured MgO) to 8–12 in bridgmanite
67 (Bdm: perovskite-structured MgSiO_3 ; Yagi et al., 1978). The high coordina-
68 tion state of Bdm, the most abundant silicate mineral in the Earth, relative
69 to co-existing phases is of particular interest. Wu et al. (2015) considered
70 the effect of coordination number increases associated with phase changes in
71 the transition zone including calculations on Bdm in the uppermost lower
72 mantle (to 24.5 GPa) but did not seek to separate the effect of coordination
73 number from bond length. We thus supplement our study of mantle phases
74 with numerical experiments designed to separate the effect of coordination
75 number and bond length on isotope fractionation in a series of hypothetical
76 oxide structured materials.

77 Whilst it is of interest to understand mineral-mineral fractionations (Huang
78 et al., 2013; Wu et al., 2015), ultimately it is of broader geological signifi-
79 cance to constrain mineral-melt fractionations, which might drive larger scale
80 isotopic differences in the Earth. For example, if crystallization of a magma
81 ocean involves phases that fractionate Mg isotopes, global Mg isotopic het-
82 erogeneities may be generated by mineral-melt segregation. Despite progress
83 with models of aqueous solutions (Rustad and Bylaska, 2006; Kowalski and
84 Jahn, 2011; Kowalski et al., 2013; Gao et al., 2018; Wang et al., 2019), and

85 more recent work on isotope fractionation in basaltic melts at low pressure
86 (Rabin et al., 2023) determinations of melt-mineral isotopic fractionations re-
87 mains challenging for first principles calculations (see Blanchard et al., 2017,
88 for a review of these methods). To circumvent this problem, previous stud-
89 ies invoked the apparent lack of Mg isotopic fractionation between olivine
90 and mafic melt at low pressure, inferred from the absence of systematic vari-
91 ability in the Mg isotopic compositions of a suite of magmas controlled by
92 addition and loss of olivine (Teng et al., 2007), to support the use of forsterite
93 (Mg_2SiO_4 : Fo) as a proxy for melt in their numerical experiments (Wu et al.,
94 2015).

95 Our treatment of the melt phase in this contribution is different in two
96 respects. Firstly, as a low pressure datum we use a recent, high-precision, di-
97 rect determination of the isotopic fractionation factor for Mg between olivine
98 and melt (Liu et al., 2022), which is discernibly less than unity. Secondly,
99 we use our experiments with different hypothetical phases with fixed MgO
100 composition, but different Mg coordination environments and variable Mg-O
101 bond lengths to produce a parameterised model of Mg isotope fractionation.
102 We argue that this approach has predictive power for phases, such as melt,
103 where only the atomic structure is known. Pinned by the new determination
104 of the fractionation factor between forsterite and melt at low pressure, we
105 then use this model, in combination with knowledge of how melt structure
106 changes with pressure (Karki et al., 2006; de Koker, 2009) to calculate Mg
107 isotope fractionation between mantle minerals and coexisting melts in a crys-
108 tallising deep magma ocean. Although rudimentary, this is the first attempt
109 to quantify the influence of pressure on melt structure in modelling isotopic

110 fractionations during the crystallisation of magma oceans.

111 **2. Methods**

112 In order to explore the effect of pressure, temperature and crystal chem-
113 istry on the fractionation of ^{24}Mg from ^{26}Mg we employed a first-principles
114 atomic-scale approach to calculate the reduced partition functions for the
115 two isotopes in Fo, Per, Bdm and five hypothetical MgO polymorphs. While
116 not directly addressing the fractionation with a high pressure melt phase,
117 we argue below that these calculations are sufficient to give the sense of
118 the fractionation behaviour when extrapolated from the known behaviour
119 at low pressure to extreme conditions not easily amenable to experiment.
120 Our approach to these calculations follows a number of previous studies (e.g.
121 Blanchard et al., 2009; Javoy et al., 2012; Li and Liu, 2011; Li et al., 2009;
122 Méheut et al., 2007, 2009; Rustad and Dixon, 2009) including examples of
123 the fractionation of Mg isotopes (Young et al., 2009; Schauble, 2011; Huang
124 et al., 2013; Wu et al., 2015; Wang et al., 2017; Duan et al., 2023; Wang
125 et al., 2023), which have established the predictive accuracy of first princi-
126 ples simulation to address isotopic fractionation. However, we believe our
127 calculations are the first to consider conditions relevant to the crystallisation
128 of a global magma ocean.

129 Key to the calculations is the definition of the reduced partition function,
130 $\beta(X, Y, Y^*)$, which is the equilibrium constant for the exchange reaction for
131 two isotopes of an element (Y and Y^*) between the material of interest,
132 denoted X , and a gas formed of dissociated, non-interacting atoms of element
133 Y (Bigeleisen and Mayer, 1947; Urey, 1947). The equilibrium fractionation

134 factor, $\alpha(X^1, X^2, Y, Y^*)$, between two crystalline phases (X^1 and X^2) is then
 135 given by the ratio of the reduced partition functions or, more conveniently,
 136 as a difference in the expected measured isotopic content:

$$\begin{aligned}
 137 \quad \Delta Y_{X^1-X^2}^* &\approx 1000 \ln (\alpha(X^1, X^2, Y, Y^*)) \\
 138 \quad &= 1000 \ln (\beta(X^1, Y, Y^*)) - 1000 \ln (\beta(X^2, Y, Y^*)), \quad (1) \\
 139
 \end{aligned}$$

140 where inclusion of the factors of 1000 means that $\Delta Y_{X^1-X^2}^*$ is the ‰ difference
 141 between the two phases. The important feature of this approach is that, for
 142 crystals and in the harmonic approximation, $\beta(X, Y, Y^*)$ can be calculated
 143 from knowledge of only the phonon density of states (Keiffer, 1982; Schauble,
 144 2004):

$$145 \quad \beta(X, Y, Y^*) = \prod_{i=1}^{N_q} \left[\prod_{j=1}^{3N_{\text{at}}} \left(\frac{\omega_{i,j}^*}{\omega_{i,j}} \frac{e^{-h\omega_{i,j}^*/(2kT)}}{1 - e^{-h\omega_{i,j}^*/(kT)}} \frac{1 - e^{-h\omega_{i,j}/(kT)}}{e^{-h\omega_{i,j}/(2kT)}} \right) \right]^{w_i}, \quad (2)$$

146 where $\omega_{i,j}$ and $\omega_{i,j}^*$ are the phonon frequencies at the i^{th} reciprocal lattice sam-
 147 pling point for the j^{th} branch in crystal X containing the Y and Y^* isotopes,
 148 respectively, T is the absolute temperature, k is the Boltzmann constant and
 149 h is the Plank constant. For a simulation cell containing N_{at} atoms, the prod-
 150 ucts run over the $3N_{\text{at}}$ modes for each of the N_q points sampled in the first
 151 Brillouin zone (the three acoustic modes at the Γ point representing trans-
 152 lations of the crystal are excluded from the product). The Brillouin zone is
 153 sampled using the scheme due to Monkhorst and Pack (1976). Symmetry of
 154 the reciprocal lattice is used to avoid the wasteful calculation of frequencies
 155 for equivalent points with weighting factors, w_i , being applied to properly
 156 account for points on the edge of the sampled irreducible volume. The com-
 157 putational task is thus to calculate $\omega_{i,j}$ and $\omega_{i,j}^*$ with sufficient accuracy to
 158 lower mantle pressure.

159 We calculate phonon frequencies using density functional perturbation
160 theory (DFPT: Baroni et al., 1987, 2001) as implemented in the CASTEP
161 code (Clark et al., 2005) using the plane-wave and pseudopotentials approach
162 (Payne et al., 1992). First, density functional theory (DFT: Hohenberg and
163 Kohn, 1964; Kohn and Sham, 1965) is used to determine the crystal structure
164 (atomic positions and cell parameters) of each crystal at target pressures in
165 10 GPa increments between -10 and 120 GPa. We adopt the generalised
166 gradient approximation (GGA) of Perdew et al. (1996) and make use of
167 norm-conserving pseudopotentials for nuclei and core electrons (only 3s and
168 3p electrons are explicitly included for Si atoms, 2p electrons for O atoms,
169 and 3s electrons for Mg atoms). Explicit valence electrons are expanded on
170 a plane wave basis with a cut-off energy of 900 eV for all three phases and
171 with the electronic band structure sampled on $3\times 3\times 3$, $4\times 2\times 4$ and $4\times 4\times 4$
172 Monkhorst-Pack grids for Bdm, Fo and Per, respectively (these parameters
173 were chosen by testing for convergence of the phonon frequencies, but repro-
174 duce the crystal structures as described below).

175 Once the equilibrium crystal structure is determined, the phonon fre-
176 quencies are given by the square root of the eigenvalues of the dynamical
177 matrix:

$$178 \quad D_{\alpha\alpha'}^{\kappa\kappa'}(\mathbf{q})\varepsilon_{j\kappa,\alpha\mathbf{q}} = \omega_{\mathbf{q},j}^2\varepsilon_{j\kappa,\alpha\mathbf{q}}, \quad (3)$$

179 which is, in turn, a function of the second derivatives of the energy of the
180 system with respect to atomic displacements:

$$181 \quad D_{\alpha\alpha'}^{\kappa\kappa'}(\mathbf{q}) = \frac{1}{\sqrt{m_{\kappa}m_{\kappa'}}} \sum_a \left(\frac{\partial^2 E}{\partial \mathbf{u}_{\kappa,\alpha} \partial \mathbf{u}_{\kappa',\alpha'}} \right) e^{-i\mathbf{q}\cdot\mathbf{R}_a}, \quad (4)$$

182 where E is the internal energy of the system, m_{κ} and $\mathbf{u}_{\kappa,\alpha}$ is the mass and

183 displacement of atom κ in direction α , \mathbf{q} is the wave vector, and the summa-
184 tion runs over the distances, \mathbf{R}_α , between periodic replicas of the two atoms.
185 The eigenvectors, ε , in Equation 3 describe how the atoms move for each
186 phonon frequency. These lattice dynamics calculations are performed using
187 variational DFPT (Gonze, 1997; Gonze and Lee, 1997) using the implemen-
188 tation described by Refson et al. (2006). An important point is that E does
189 not depend on the masses of the atoms in the crystal. This property can be
190 used to minimise the number of DFPT calculations needed to evaluate the
191 reduced partition function by storing the matrix of second derivatives and
192 reusing this for both isotopic substitutions. The ‘phonons’ utility, distributed
193 with CASTEP, allows this optimisation alongside Fourier interpolation (Gi-
194 annozzi et al., 1991), which allows phonon frequencies to be estimated at
195 wave vectors between those included in the DFPT calculation. We note that
196 under all the conditions we consider the DFPT calculations yield real eigen-
197 values for all phases indicating that they are dynamically (but not necessarily
198 thermodynamically) stable.

199 Our calculations of isotope fractionation in hypothetical MgO polymorphs
200 are designed to allow us to explore the relative importance of local bond-
201 ing environment (bond length and coordination number) and chemistry on
202 the equilibrium fractionation of Mg isotopes. We thus performed DFT and
203 DFPT calculations on a range of prototypical ‘MX’ structures with small,
204 high symmetry unit cells and fixed MgO composition but with the Mg atom
205 occupying different coordination sites. In each case we first optimised the
206 crystal structure while constraining symmetry at 0 GPa before building a
207 super-cell, calculating the dynamical matrix, and evaluating the reduced par-

208 titution coefficients following the approach outlined above. This process gives
209 us access to calculated bond lengths and reduced partition coefficients for
210 each structure considered. For these calculations we considered five struc-
211 tures in addition to Per: the cubic and hexagonal ZnS structures, the NiAs
212 structure and its ‘inverse’, and the primitive cubic CsCl structure. Many
213 of these MgO polymorphs have small unit cells, minimising the computa-
214 tional cost of these experiments. When calculating the change in vibration
215 behaviour due to the substitution of ^{26}Mg for ^{24}Mg , we attempt to keep the
216 distance between substituted sites the same. To do this we use the conven-
217 tional cubic unit cell for the rock salt structure, a $2\times 2\times 2$ supercell for the
218 CsCl structure and $2\times 2\times 1$ supercells for the NiAs and ZnS structures. In
219 order to probe the relationship between bond length and Mg isotope frac-
220 tionation we also scaled the lattice vectors after optimisation, increasing or
221 decreasing their length as needed to set the bond length before calculation of
222 the dynamical matrix. We use these scaled structures to calculate reduced
223 partition functions for crystals with the same structure and Mg coordina-
224 tion number but with different bond lengths. While this scaling results in
225 structures with negative or very high fictive pressures, it means that the
226 bond lengths for different structures and coordination numbers overlapped,
227 enabling us to decouple the effect of bond length from that of coordination
228 number.

229 **3. Results**

230 The primary aim of our DFPT calculations is to establish the phonon
231 frequencies across the irreducible wedge of the Brillouin zone for Fo, Per

232 and Bdm at pressures between -10 and 120 GPa in order to allow the cal-
 233 culation of the reduced partition functions. Our strategy for choosing the
 234 electronic parameters of the calculations that need to be converged (k-point
 235 sampling and plane wave cut-off) was to increase these until the frequency
 236 of the Γ point optic modes changed by less than 0.5 cm^{-1} . This also gives
 237 suitably converged lattice parameters (Table 1) and atomic positions. As
 238 expected given the use of a GGA functional, these values are larger than
 239 the experimentally determined cell parameters. This makes little difference
 240 to the calculated reduced partition functions. Comparison with results from
 241 the local-density approximation, which underestimates the cell parameters,
 242 shows that the calculated reduced partition functions are not strongly modi-
 243 fied by choice of functional. Convergence of the numerical parameters in the
 244 calculation is a more important effect.

Table 1: Calculated lattice parameters of Fo, Per and Bdm as a function of pressure
 from static lattice minimisation. A parametrisation of the volume with temperature and
 pressure derived from lattice dynamics and DFPT can be found in the SI.

Phase and lattice parameter	0 GPa	25 GPa	50 GPa	120 GPa
Per, a (\AA)	4.25	4.08	3.97	3.77
Fo, a (\AA)	4.80	4.64	4.55	4.41
Fo, b (\AA)	10.32	9.67	9.27	8.48
Fo, c (\AA)	6.05	5.73	5.55	5.27
Bdm, a (\AA)	4.83	4.68	4.56	4.33
Bdm, b (\AA)	4.98	4.85	4.76	4.60
Bdm, c (\AA)	6.97	6.75	6.60	6.31

245 The number of reciprocal space sampling points in Equation 2, the ‘q-

246 point sampling', must also be sufficiently large to allow the calculated reduced
247 partition functions to converge. For Per we find that sampling only the Γ
248 point results in an underestimate of $1000 \ln(\beta(\text{Per}, {}^{24}\text{Mg}, {}^{26}\text{Mg}))$ relative to
249 the fully converged case by almost 2‰ at 300 K even if Fourier interpola-
250 tion is used to add a dense grid of additional points. Sampling on a $3 \times 3 \times 3$
251 Monkhorst-Pack grid gives convergence better than 0.1‰ and interpolating
252 onto a $7 \times 7 \times 7$ grid better than 0.01‰ convergence at 300 K. This behaviour
253 mirrors that reported by Schauble (2011) and we perform a similar con-
254 vergence analysis to calculate reduced partition functions for the other two
255 phases such that, at the temperatures of interest, results are fully converged.

256 A further adjustable parameter which appears to have received less atten-
257 tion is the separation of adjacent substituted isotopes in the periodic models.
258 As pointed out by Méheut et al. (2007), Equation 2 is derived under the as-
259 sumption that isotopic substitutions are in the dilute limit where the free
260 energy change associated with a substitution on a particular site does not
261 depend on the separation between the site and its periodic images. We in-
262 vestigated the convergence of the reduced partition function with increasing
263 separation in Per as shown in Table 2. We find that convergence for this
264 material is rather slow and, for the range of simulation cell sizes probed, that
265 there may still be an error of ~ 0.1 ‰ at 300K. Unfortunately, the compu-
266 tational cost of the DFPT calculations grows very quickly as the separation
267 between isotope images grows and this prevents a more detailed analysis of
268 this source of error for any of the phases considered here. However, given the
269 simulation cells used in our calculations (a $2 \times 2 \times 2$ primitive super cell for
270 Per with a $4 \times 4 \times 4$ q-point sampling and the conventional orthorhombic cells

271 for Fo and Bdm with $3 \times 1 \times 3$ and $3 \times 3 \times 3$ q-point sampling, respectively) we
 272 believe that all our calculations are converged to much better than 0.01 %
 273 at temperatures above 1000 K.

Table 2: Convergence in calculated reduced partition function, $1000 \ln(\beta(\text{Per}, {}^{24}\text{Mg}, {}^{26}\text{Mg}))$, at 300 K in Per with increasing separation between adjacent isotopically substituted magnesium atoms.

Mg* – Mg* separation (Å)	Reduced partition function (‰)	Simulation cell	Fraction of Mg atoms substituted
3.01	25.76	primitive	100%
4.25	27.67	conventional	25 %
6.02	26.13	$2 \times 2 \times 2$ primitive	12.5 %
8.51	26.38	$2 \times 2 \times 2$ conventional	3.125 %

274 We express the temperature dependence of the reduced partition func-
 275 tions by fitting the computed values to a convenient polynomial equation
 276 also used by Schauble (2011) and Huang et al. (2013):

$$277 \quad 1000 \ln(\beta(T)) = AT^{-6} + BT^{-4} + CT^{-2}, \quad (5)$$

278 where A , B and C are fitted constants given for the three phases at each
 279 pressure in Table 3. We compare our results with those of Schauble (2011),
 280 Huang et al. (2013) and Wu et al. (2015) in Figure 1 and, overall, find good
 281 agreement with previous work. In particular, all results for Fo are consis-
 282 tent and this is despite the differences in the choice of exchange-correlation
 283 functional (we use a GGA while most previous work makes use of the local-
 284 density approximation). The very non-linear behaviour of the results from
 285 Huang et al. (2013) below 400 K is because these workers only parametrise

286 their model using results at higher temperatures. Similarly, the more linear
287 behaviour of the results of Wu et al. (2015) is because these authors fit to a
288 lower order polynomial than that used here. Given the excellent agreement
289 for Fo, explaining the somewhat larger difference between the results of re-
290 cent studies of Per and Bdm is not trivial. For Per some of the difference can
291 be attributed to the separation of periodic images of the isotopic substitu-
292 tion. This convergence is not smooth (see Table 2) but the 1.3 ‰ difference
293 at 300 K for changing the separation from 4.25 Å to 8.51 Å would explain a
294 large portion of the discrepancy. A more general source of the difference can
295 be attributed to the different choice of exchange-correlation functional. This
296 would imply that this has a more important role for Bdm than Per or Fo,
297 but the reason why this would be the case is not obvious. Nevertheless, given
298 the differences in the details of the methodology, the agreement between the
299 different studies is remarkable, and at least indicates that geochemical pre-
300 dictions derived from these calculations have value where experiments have
301 not been carried out. Figure 1 also shows the effect of pressure on the re-
302 duced partition functions. In all cases, and in common with the results of
303 Wu et al. (2015), pressure acts to increase the calculated reduced partition
304 function and thus counteract the effect of temperature. We show how these
305 changes with temperature and pressure interact to give variations in the ex-
306 pected equilibrium isotopic fractionation in Figure 2 where the variations
307 in $1000 \ln (\alpha(\text{Per}, \text{Fo}, {}^{24}\text{Mg}, {}^{26}\text{Mg}))$ and $1000 \ln (\alpha(\text{Bdm}, \text{Fo}, {}^{24}\text{Mg}, {}^{26}\text{Mg}))$ are
308 shown.

Table 3: Fitted constants for $1000 \ln(\beta(T)) = AT^{-6} + BT^{-4} + CT^{-2}$ (Equation 5) giving a parameterisation of $1000 \ln(\beta(X, {}^{24}\text{Mg}, {}^{26}\text{Mg}))$ as a function of temperature in the harmonic approximation for crystal cell parameters optimised at different applied pressures.

	A (K^6)	B (K^4)	C (K^2)
Per, 0 GPa	1.3325×10^{14}	-1.4605×10^{10}	2.4985×10^6
Per, 25 GPa	2.8276×10^{14}	-2.7247×10^{10}	3.6338×10^6
Per, 50 GPa	5.3100×10^{14}	-4.3427×10^{10}	4.6299×10^6
Per, 120 GPa	2.0417×10^{15}	-1.1163×10^{11}	7.0470×10^6
Fo, 0 GPa	1.8414×10^{14}	-1.6279×10^{10}	2.4312×10^6
Fo, 25 GPa	4.9086×10^{14}	-3.6942×10^{10}	3.7982×10^6
Fo, 50 GPa	9.6399×10^{14}	-6.2194×10^{10}	4.9505×10^6
Fo, 120 GPa	3.0675×10^{15}	-1.5004×10^{11}	7.7714×10^6
Bdm, 0 GPa	2.0352×10^{14}	-1.6193×10^{10}	2.2502×10^6
Bdm, 25 GPa	3.8318×10^{14}	-2.7832×10^{10}	3.1142×10^6
Bdm, 50 GPa	6.4226×10^{14}	-4.2223×10^{10}	3.9157×10^6
Bdm, 120 GPa	1.7920×10^{15}	-9.4452×10^{10}	5.9946×10^6

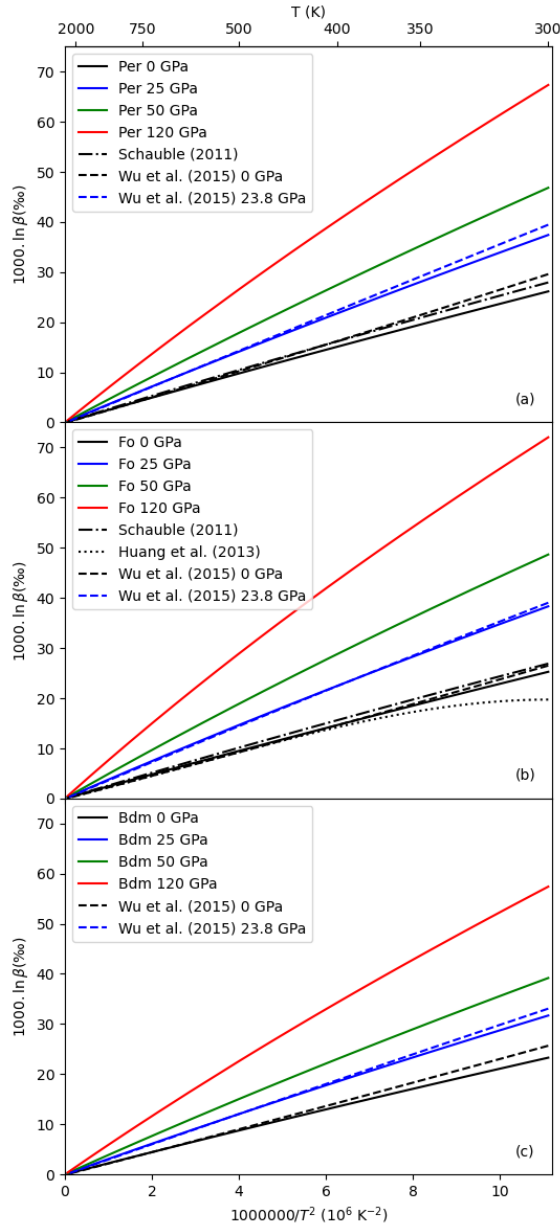


Figure 1: Calculated reduced partition functions for (a) Per, (b) Fo and (c) Bdm as a function of temperature at pressures of 0 (black), 25 (blue), 50 (green) and 120 (red) GPa. In all cases the reduced partition functions increases with increasing pressure and decreasing temperature. Previously published results are also shown using the same colour scale for comparison. Schauble (2011): dot-dashed lines; Huang et al. (2013): dotted line; Wu et al. (2015): dashed lines (showing results at 0 and 23.8 GPa).

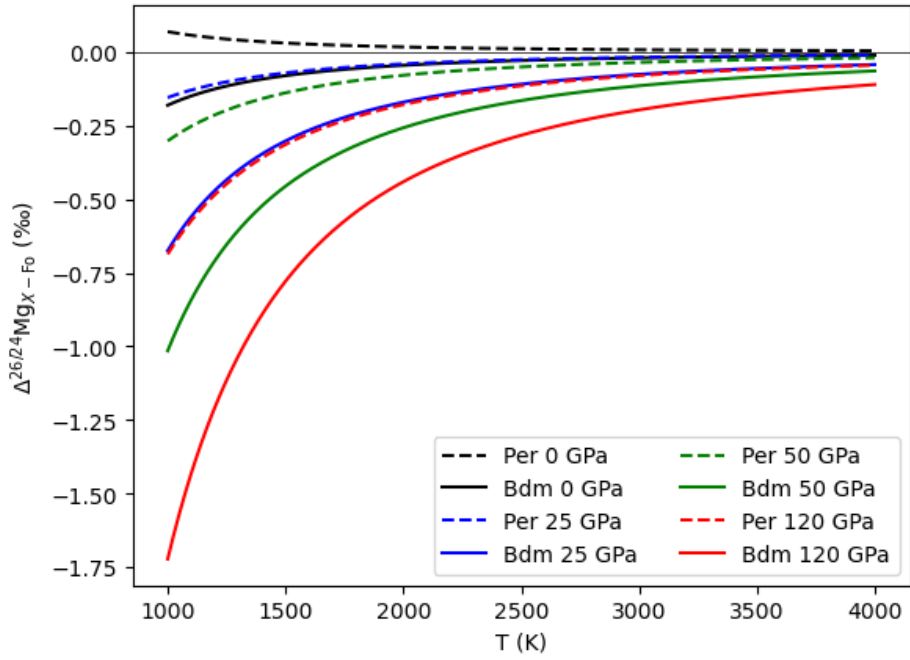


Figure 2: Calculated equilibrium partitioning between Fo and Bdm (solid lines) or Per (dashed lines) as a function of temperature and cell volume for fixed sized simulation cells corresponding to static lattice optimisation (i.e. at 0 K, and neglecting the zero-point energy) at 0 (black), 25 (blue), 50 (green) and 120 (red) GPa.

309 *3.1. Structural controls on isotope fractionation*

310 The equilibrium fractionation factor between Fo (or Per) and Bdm in-
311 dicates that Bdm will always tend to preferentially incorporate isotopically
312 lighter Mg when in equilibrium with the phases with six coordinate Mg. At 0
313 GPa and 1000 K this effect, if fully expressed, should result in a measurable
314 relative difference of $^{26}\text{Mg}/^{24}\text{Mg}$ between Fo and Bdm ($\Delta^{26/24}\text{Mg}_{\text{Fo-Bdm}}$) of
315 nearly 0.2 ‰. Increasing temperature rapidly reduces the fractionation but
316 increasing pressure counteracts this effect: at 50 GPa $\Delta^{26/24}\text{Mg}_{\text{Bdm-Fo}}$ is
317 more negative than -0.2 ‰ to about 2500 K. The predicted fractionation be-
318 tween Per and Fo is considerably smaller. At 0 GPa the heavier Mg isotopes
319 are predicted to be preferentially incorporated into Per but pressure reverses
320 this trend with the heavier isotopes preferred by Fo at 25 and 50 GPa. At all
321 pressures the expected fractionation between the two six coordinate phases
322 is smaller than that between the six coordinate phases and the more highly
323 coordinate site in Bdm. This strong effect of Mg coordination number is
324 reminiscent of the results of Huang et al. (2013), who found that phases
325 with six coordinate Mg (forsterite, diopside and enstatite) only weakly dif-
326 ferentiate between ^{24}Mg and ^{26}Mg , but that these phases become enriched
327 in the heavier Mg isotopes compared to pyrope and majorite garnet, both
328 with eight coordinate Mg. In common with our results, Huang et al. (2013)
329 and Wu et al. (2015) also found that increasing pressure acts to increase
330 this fractionation between phases with different Mg coordination numbers,
331 an effect that can be explained by the different compressibility of sites with
332 different coordination environments. This is in contrast to the case of silicon
333 in which there is little influence of pressure in isotopic fractionation between

334 mantle phases (Huang et al., 2014). However, these changes in coordination
335 number are accompanied by changes in bond length, which are expected to
336 alter the vibrational frequencies and thus isotope fractionation. It is unclear
337 from our results on mantle phases whether coordination number or bond
338 length is the dominant structural control on Mg isotope fractionation and
339 we performed numerical experiments using hypothetical MgO polymorphs
340 designed to resolve this.

341 We consider Mg in six different structural environments. In the cubic
342 and hexagonal ZnS structures Mg is tetrahedrally coordinated with our 0
343 GPa DFT calculations giving an Mg – O bond length of about 2.0 Å. The
344 difference between these structures is in the stacking of layers of tetrahedra
345 which means the structures have different second coordination shells around
346 the isotopically substituted Mg. In the rock salt (Per) and NiAs structures
347 Mg sits within six coordinate sites with calculated Mg – O bond lengths
348 of about 2.1 Å. The octahedra in Per share corners while octahedra in the
349 NiAs structure share faces and edges. The NiAs structure has a second site
350 where Mg is in trigonal prismatic coordination. In this structure all edges are
351 shared. Finally, in the primitive cubic CsCl structure Mg is eight coordinate
352 with calculated Mg – O bond lengths of about 2.3 Å and with all faces shared
353 between adjacent polyhedra. Key structural parameters at 0 GPa and the
354 calculated reduced partition functions for these structures are given in Table
355 4.

356 We parameterise the effect of temperature on the reduced partition func-
357 tions of the six MX structures in the same way as we treated the results
358 for mantle phases presented above. Parameters of these fits are shown in

Table 4: Calculated summary structural parameters of hypothetical MgO crystal structures showing controls on $1000 \ln (\beta(X, {}^{24}\text{Mg}, {}^{26}\text{Mg}))$ at 300 K

	Mg coordination number	Mg – O bond lengths (Å)	Mg* – Mg* separation (Å)	300 K reduced partition function (‰)
hexagonal ZnS structure	[4]	1.995	5.134	30.14
cubic ZnS structure	[4]	2.000	5.641	30.05
NaCl structure (periclase)	[6]	2.127	6.017	26.13
NiAs structure (octahedral)	[6]	2.140	5.158	26.06
NiAs structure (trigonal prismatic)	[6]	2.153	5.233	23.18
CsCl structure	[8]	2.302	5.317	18.12

359 Table 5 with the reduced partition functions shown in Figure 3. It appears
 360 from inspection of Table 4 and Figure 3 that the structure of the first coordi-
 361 nation shell explains almost all of the variability in partitioning between
 362 these simple hypothetical structures with identical chemistry. At least for
 363 these systems, the nature of the second coordination shell, and the shar-
 364 ing of corners, edges and faces between coordination polyhedra is relatively
 365 unimportant. However, this analysis does not account for the variability in
 366 bond lengths between structures with different coordination number at the
 367 same pressure.

Table 5: Fitted constants for $1000 \ln(\beta(T)) = AT^{-6} + BT^{-4} + CT^{-2}$ (Equation 5) giving a parameterisation of $1000 \ln(\beta(X, {}^{24}\text{Mg}, {}^{26}\text{Mg}))$ as a function of temperature in the harmonic approximation for hypothetical MgO crystal structures optimised at 0 GPa.

	A (K^6)	B (K^4)	C (K^2)
hexagonal ZnS structure	2.2580×10^{14}	-2.1812×10^{10}	2.9271×10^6
cubic ZnS structure	2.2551×10^{14}	-2.1729×10^{10}	2.9183×10^6
NaCl structure (periclase)	1.3325×10^{14}	-1.4605×10^{10}	2.4985×10^6
NiAs structure (octahedral)	1.5567×10^{14}	-1.6076×10^{10}	2.5052×10^6
NiAs structure (trigonal prismatic)	9.9342×10^{13}	-1.1700×10^{10}	2.2039×10^6
CsCl structure	9.3173×10^{13}	-1.0320×10^{10}	1.7341×10^6

368 To distinguish between true coordination effects and the effect of different
 369 bond lengths we vary these independently by scaling the lattice vectors of five
 370 of the hypothetical MgO polymorphs (omitting the hexagonal ZnS structure
 371 as it is so similar to the cubic ZnS structure). This allows us to calculate the
 372 reduced partition function for different bond lengths in otherwise identical
 373 structures as shown in Figure 4. In this analysis structures with low coordi-

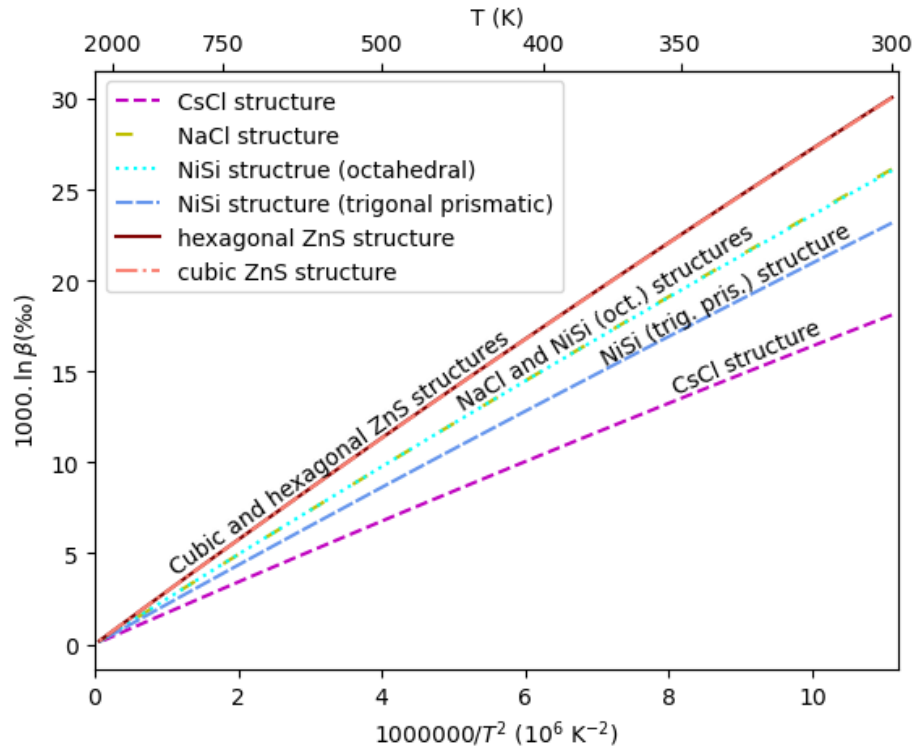


Figure 3: Calculated reduced partition functions for various MX structures with fixed MgO composition (see text for discussion). In common with the silicates, structures with low Mg coordination number (e.g. the ZnS structures with four coordinate Mg shown in overlapping red colours) consistently show a larger value of β than structures with high Mg coordination number (e.g. the eight coordinate CsCl structure, shown in purple). Values of β for structures with Mg in octahedral coordination (greens) or other six coordinate Mg environments (blue) fall between these upper and lower values.

374 nation number and large bond lengths correspond to situations with negative
375 pressure while small bond lengths for structures with high coordination num-
376 bers correspond to situations with positive pressure (e.g. the largest bond
377 length for cubic ZnS in Figure 4 corresponds to a pressure of -20.6 GPa and
378 the smallest bond length for the CsCl structure corresponds to a pressure of
379 86.7 GPa).

380 Results of these calculations show a clearly separated effect of both bond
381 length and coordination number on the reduced partition function. A re-
382 duction in bond length for a given coordination number (e.g. by increasing
383 pressure) increases the reduced partition function (i.e. leads to an increased
384 preference for heavy isotopes). For example, for cubic ZnS in Figure 4 re-
385 ducing the bond length from ~ 2.3 Å to ~ 2.0 Å increases $1000 \ln \beta$ from
386 $\sim 10\%$ to $\sim 30\%$ at 300 K. In contrast, reducing the coordination number
387 for a given bond length decreases the reduced partition function. For exam-
388 ple, in Figure 4 at a bond length of ~ 2.2 Å moving from a coordination
389 number of 4 (cubic ZnS) to 8 (CsCl) increases $1000 \ln \beta$ from $\sim 15\%$ to
390 $\sim 30\%$ at 300 K. For a given pressure increasing the coordination number
391 increases the bond length and this effect can be significant. For example,
392 the data points highlighted by large circles and corresponding to the 0 GPa
393 bond lengths in Figure 4 show a decrease in reduced partition function with
394 increasing coordination number. This decrease in reduced partition function
395 with increasing coordination is due to the effect of coordination on bond
396 length. In contrast to the clear effect of bond length and coordination num-
397 ber, we see little evidence of mineral chemistry playing a significant role for
398 Mg isotope fractionation: our results for Bdm and Fo closely follow the trends

399 established by the MgO polymorphs with the same coordination numbers.
400 We note that the trend shown in Figure 4 shows a similar general trend to
401 that found for Ca by Xiao et al. (2022) but that our results for Mg show
402 none of the mixing between structures with different coordination numbers
403 and less scatter than Xiao et al.'s results for Ca. This is likely to be due
404 to the different coordinating anions (O, F, S and P) and wider range struc-
405 tures, including solid solutions, in Xiao et al.'s dataset. The extent to which
406 a wider range of crystal chemistry would alter our findings for Mg isotopic
407 fractionation in silicates remains to be determined.

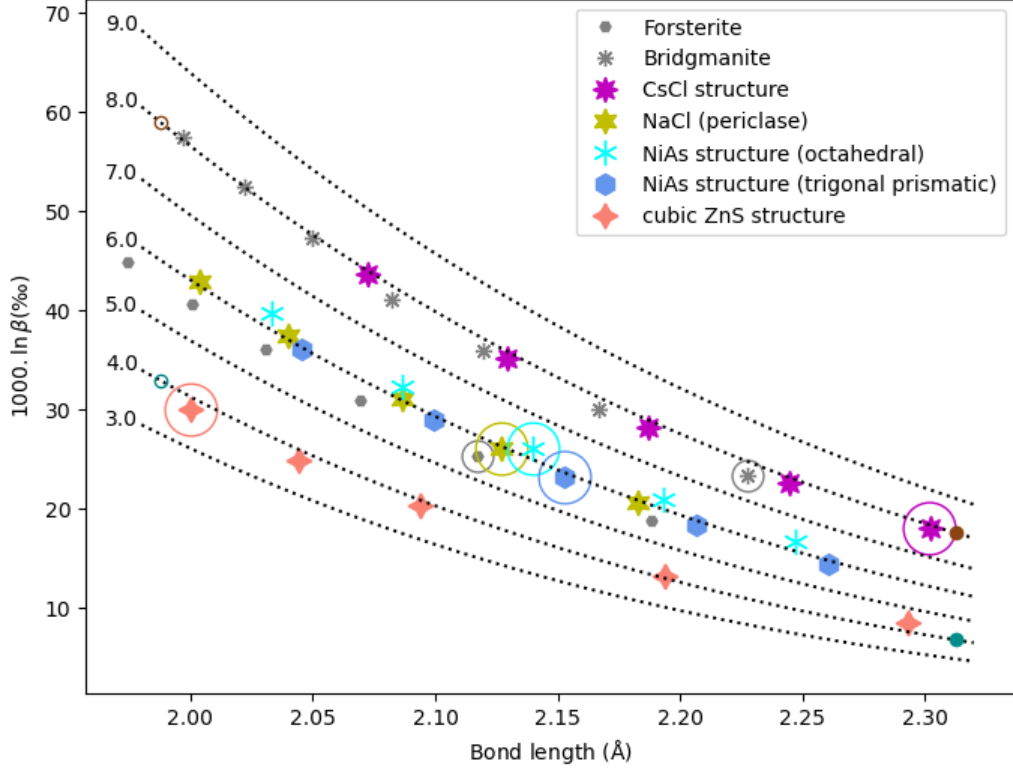


Figure 4: Large symbols: reduced partition functions at 300 K for a range of MX structured material with composition MgO and different bond lengths set by scaling the lattice parameters (see text for details). Number of sides or points on each symbol indicates the coordination number and the large circles mark the bond length at 0 GPa. Grey symbols: Fo (bond lengths corresponding to pressures between -10 and 50 GPa) and Bdm (bond lengths corresponding to pressures between 0 and 120 GPa). Dotted lines show the predictions of the fitted model with the numbers on each line referring to the coordination number. Small filled and unfilled circles show the models illustrated in Figure 8.

408 *3.2. The effect of thermal expansion on isotope fractionation*

409 For all the results described so far we have neglected the effect of thermal
410 expansion on phonon frequencies and thus on isotopic fractionation. To inves-
411 tigate the importance of this we must go beyond the harmonic approximation
412 and consider the differential thermal expansion of the phases. This effect is
413 most naturally captured using the statically constrained quasi-harmonic ap-
414 proximation (e.g. Wentzcovitch et al., 2010), because this can make use of
415 the same DFPT calculations performed to evaluate the isotopic fractiona-
416 tion. Similarly to Wang et al. (2023), for each cell volume, V , (found by
417 performing variable cell geometry optimisation with an applied pressure but
418 neglecting the effect of temperature) we calculate the phonon frequencies and
419 use these to evaluate the Helmholtz free energy. As described in the SI, the
420 resulting volume – energy data is used to fit isothermal third-order Birch–
421 Murnaghan equations of state (EOS) with the temperature dependence of
422 the EOS parameters defined by fifth order polynomials. Because pressure
423 is the derivative of the Helmholtz free energy with respect to volume, we
424 can use these equations of state to evaluate the cell volume as a function of
425 temperature and pressure (Figure 5).

426 We also evaluated β as a function of temperature at each cell volume and
427 fit this data to a polynomial in volume and temperature (polynomial coeffi-
428 cients are tabulated in the SI). In order to evaluate the equilibrium fraction-
429 ation factor as a function of pressure and temperature (for example, along
430 a geotherm) we first evaluate the cell volume for each phase, then evaluate
431 β at that volume and temperature for each of the phases. In common with
432 previous results (e.g. Wang et al., 2023) the inclusion of thermal expansion

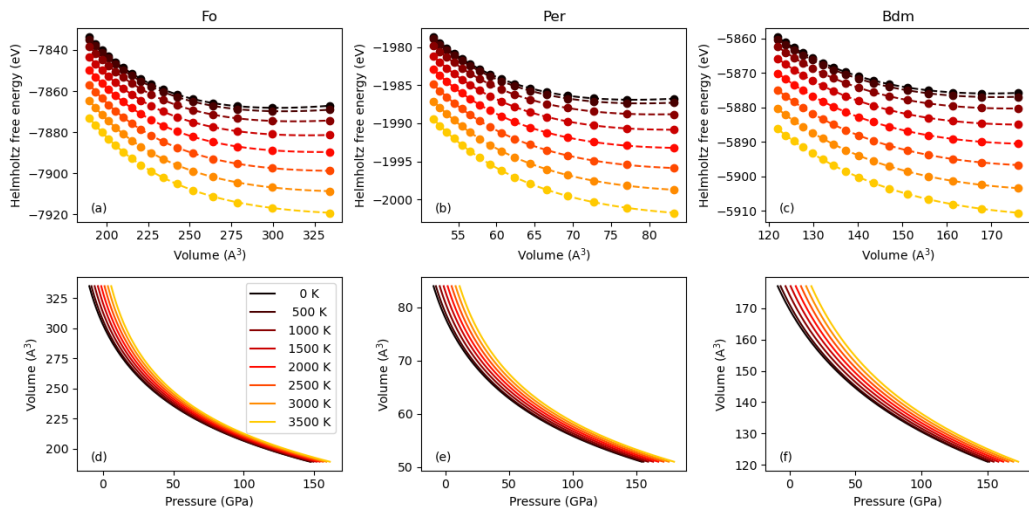


Figure 5: Isothermal third-order Birch–Murnaghan equations of state (dashed lines) fitted to lattice dynamics calculations of energy as a function of cell volume (circles) for Fo (a), Per (b), and Bdm (c) at eight temperatures. These are used to give the cell volume as a function of pressure and temperature (d – f) and incorporate thermal expansivity into our models.

433 always reduces our estimate of β . However, conditions in a global magma
434 ocean involve large compression and high temperatures such that fraction-
435 ation between phases will depend on the balance of relative compressibility
436 and thermal expansion. This is shown in Figure 6 where we compare results
437 from the evaluation of Equation 1 using the quasi-harmonic approach with
438 the results derived by neglecting thermal expansion at different depths in
439 the Earth. We have used the chondritic liquidus of Andraut et al. (2011) as
440 our geotherm. This choice, while not representing the likely conditions with
441 depth in the Earth at any point in time, gives a maximum temperature for
442 equilibration, and thus a lower bound on the fractionation factor between
443 the three phases. Even at the relatively high temperatures considered here
444 the difference between Bdm and the six coordinate phases is still significant.
445 The correction due to differential thermal expansion is rather small but is
446 potentially important (up to $\sim 0.02\%$) with, for this choice of geotherm, a
447 maximum in the fractionation factor between Fo and Bdm $> 0.1\%$ at depths
448 corresponding to the upper part of the lower mantle.

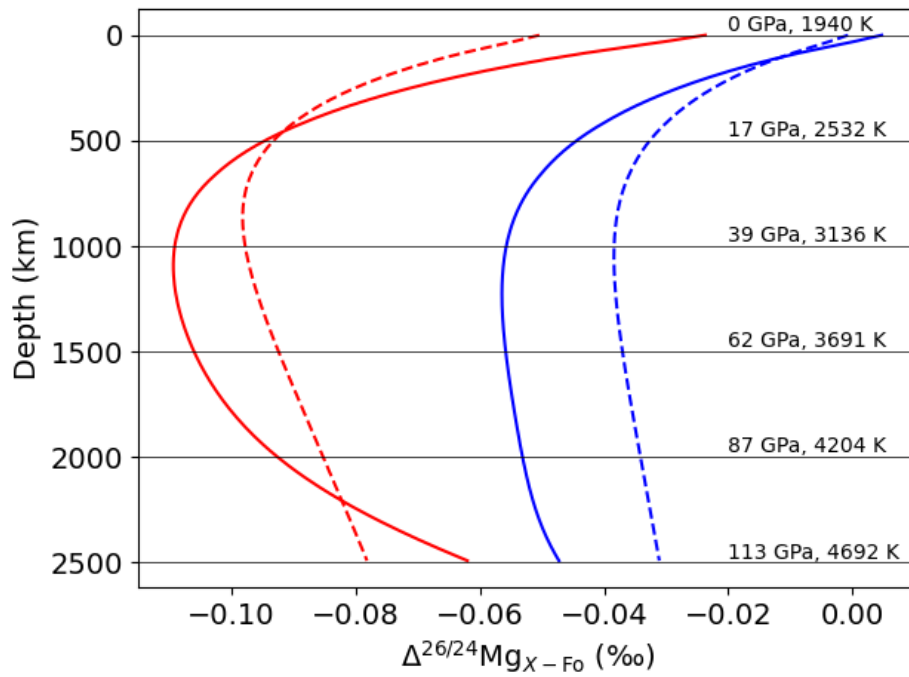


Figure 6: Calculated equilibrium partitioning between Fo and Bdm (red lines) or Per (blue lines) as a function of depth (right axis) along a chondritic liquidus. Dashed lines neglect thermal expansion. The pressure and temperature of the chondritic liquidus at selected depths is indicated numerically towards the right hand side of the figure. In this plot the reference Fo structure evolves with pressure and, for the solid lines, temperature.

449 4. Discussion

450 Our calculations have shown that equilibration between solid Bdm and
451 either Per or Fo leads to a mass-dependent fractionation of ^{24}Mg from ^{26}Mg
452 and that this effect is significant to temperatures extending well into the
453 lower mantle. This equilibrium fractionation is caused by differences in coordination
454 altering the equilibrium bond lengths in the phases and this coupled
455 effect outweighs the direct variation in fractionation caused by the change
456 in coordination alone. Overall this results in 8–12 coordinate Mg in Bdm
457 becoming relatively enriched in the lighter Mg isotopes compared to 6 coordinate
458 Mg in Per or Fo. The coupled effect of coordination and bond length
459 on fractionation leads to the possibility of fractionation of Mg isotopes between
460 Bdm and a coexisting melt phase during crystallisation of a global
461 magma ocean if Mg in the melt has a different coordination and/or bond
462 length than Mg in Bdm.

463 The structure and properties of silicate liquids have been the subject of
464 study using density functional theory combined with molecular dynamics
465 (e.g. Stixrude and Karki, 2005). These simulations allow the bond length
466 and coordination of Mg in silicate melts under the temperature, pressure
467 and chemical conditions relevant to a global magma ocean to be determined.
468 In pure liquid MgO, the average Mg coordination number is found to be 4.5–
469 5 at low pressure. This increases with increasing pressure reaching about
470 6 at 60 GPa and 7 above 150 GPa (Karki et al., 2006). In liquid silicates,
471 Mg coordination number depends on composition and is between 4 and 6 at
472 low pressure and increases with increasing pressure. For example, in liquid
473 Mg_2SiO_4 at 4000 K the coordination number is around 5 with a bond length

474 of around 1.96 Å at 0 GPa and this changes to a coordination number of
475 6.5 with a bond length of around 1.92 Å at 60 GPa (de Koker et al., 2009).
476 In CaMgSi₂O₆ the coordination number is higher, around 6 at 0 GPa in-
477 creasing to ~7.5 by 60 GPa (Sun et al., 2011). In general the coordination
478 number tends to decrease slightly with decreasing temperature or with the
479 addition of hydrogen, but both effects become less important at pressures
480 above about 20 GPa (Mookherjee et al., 2008). Overall, at depths > 700 km
481 we expect Mg silicate liquids in a crystallising magma ocean to have lower
482 coordination number and shorter bond lengths than that in the coexisting
483 liquidus phase, which is Bdm. In order to make semi-quantitative predictions
484 of this fractionation we parameterise the mean Mg–O bond lengths and Mg
485 coordination numbers for liquid Mg₂SiO₄ reported in de Koker et al. (2009)
486 and shown in Figure 7. We then use these as input for an ‘ionic model’ and
487 predict the reduced partition function for Mg in the melt as described below.

488 *4.1. An ionic model of fractionation in silicate melts*

489 Even with average structural information of the melt in hand, quantifying
490 the isotopic fractionation between crystals and liquid in a cooling magma
491 ocean is not trivial because of the lack of both appropriate empirical data
492 and DFT simulations investigating isotope fractionation in liquids. However,
493 as we detail below, we can estimate the crystal-liquid fractionation using
494 empirical data for olivine-liquid fractionation of Mg isotopes at atmospheric
495 pressure in combination with a first order model of the pressure effect on the
496 force constant of Mg-O bonds in ultramafic silicate liquid. Liu et al. (2022)
497 have recently shown empirically that ²⁶Mg/²⁴Mg ratios in olivine (Fo₈₂) are
498 0.071‰ lower than in the glass of the basaltic lavas they crystallised from

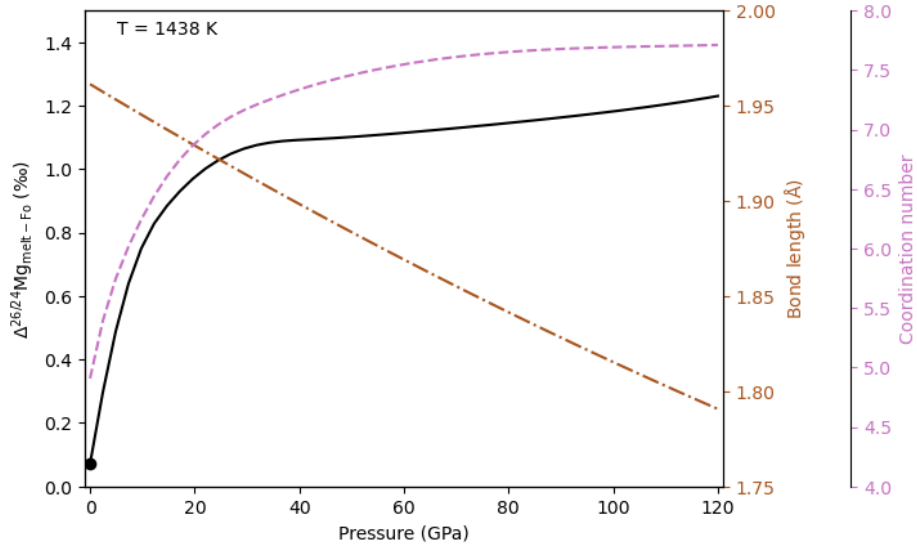


Figure 7: Predicted fractionation between liquid Mg_2SiO_4 and Fo as a function of pressure (black, left axis) from an ionic model based on melt structure data from de Koker et al. (2009) pinned to the observed fractionation between Fo and melt at ambient pressure (black dot). The fractionation shown does not account for pressure-induced changes in the structure of Fo such that isotopic composition of the melt shown here is always with respect to Fo at 0 GPa and 1438 K. Bond lengths are parameterised by a polynomial (brown, inner right axis) and coordination numbers by piecewise cubic splines (mauve, outer right axis) as described in the SI. In order to reproduce the ambient pressure measurement, the pressure used to evaluate the melt bond length and coordination number is reduced by 7.8 GPa compared to that used for solid phases.

499 at 1438 K, as qualitatively expected from the higher coordination number of
 500 Mg in olivine compared to low pressure silicate melt. There is currently no
 501 empirical evidence that variation in (ultra-)mafic silicate liquid composition
 502 affects isotopic fractionation but given the increasing coordination number
 503 of Mg in silicate liquid, we cannot assume that $^{26}\text{Mg}/^{24}\text{Mg}$ ratios in (ultra-
 504)mafic silicate liquid remain constant to lower mantle pressures. Instead,
 505 we build an ‘ionic’ model following the approach of Young et al. (2015) but
 506 making modifications to fit the DFT results presented above. This class of
 507 models assume the vibrational behaviour of Mg atoms can be described by
 508 an effective Born–Mayer type interatomic potential:

$$E(r) = \frac{z_1 z_2}{r} \left(\frac{e^2}{4\pi\epsilon_0} \right) + \frac{b}{r^n}, \quad (6)$$

509 which gives the bonding energy, E , as a function of the mean distance be-
 510 tween Mg and O ions, r . The first term in Equation 6 represents Coulomb
 511 interactions and the second represents repulsion due to the overlap of elec-
 512 tron clouds. Balancing these terms gives an equilibrium bond length, r_0 ,
 513 which minimises E . The parameters z_1 and z_2 represent the charges on the
 514 ions, e is the charge of an electron, and ϵ_0 is the vacuum permittivity. The
 515 parameters b and n define the strength and shape of the repulsion term.

516 In the ionic model, the vibrational properties and thus isotopic fractiona-
 517 tion are determined from the effective force constant K_f , which is the second
 518 derivative of Equation 6 evaluated at r_0 :

$$K_f = \left. \frac{d^2 E}{dr^2} \right|_{r=r_0} = \frac{z_1 z_2 e^2 (1 - n)}{4\pi\epsilon_0 r_0^3}, \quad (7)$$

519 with n treated as an adjustable parameter (commonly set to 12), formal
 520 charges assumed, and where b is written in terms of the equilibrium bond

521 length ($b = -(e^2/4\pi\epsilon_0) z_1 z_2 / nr_0^{n-1}$) and eliminated. This allows calculation of
 522 the reduced partition function:

$$\beta = 1 + \frac{1}{24} \left(\frac{h}{k_B T} \right)^2 \frac{K_f}{4\pi^2} \left(\frac{1}{m} - \frac{1}{m'} \right). \quad (8)$$

523 Following Young et al. (2015) the model described by Equations 6-8 only
 524 depends on the ionic charges and the bond length. While the model yields the
 525 general trend of an increase in the reduced partition function with decrease
 526 in bond length showing in Figure 4 it does not predict the calculated reduced
 527 partition functions derived from the DFT calculations. It is also unable to
 528 capture the dependence of reduced partition function on coordination num-
 529 ber. Indeed, we find that no single value of n or choice of ionicity, ζ , to scale
 530 the charges (i.e. $z_1 = \zeta \times 2.0$ and $z_2 = \zeta \times -2.0$), gives a good fit to the results
 531 presented in Figure 4, even for a single coordination number. We therefore
 532 choose to extend the model by making ζ a function of equilibrium bond
 533 length and coordination number, n_c , allowing a model with three adjustable
 534 parameters: $\zeta = \zeta_0 + r_0 \zeta_r + n_c \zeta_c$. We fit these parameters to the calculated
 535 reduced fractionation factors for all hypothetical MgO polymorphs at 300 K
 536 fixing n at 12. This is reminiscent of the approach of Young et al. (2009) and
 537 Sossi and O'Neill (2017), who replaced z_i in Equation 7 with the mean bond
 538 strength (z_i divided by the coordination number). Their approach makes K_f
 539 a function of coordination number of the cations and the anions but Young
 540 et al. (2015) report that this generally underestimates fractionation factors.
 541 Our more flexible model, shown by the dotted lines in Figure 4, is able to
 542 reproduce the calculated variation in bond-length and coordination number.
 543 As well as fitting the DFT calculations, this prescription gives reasonable
 544 effective potentials and effective charges (Figure 8).

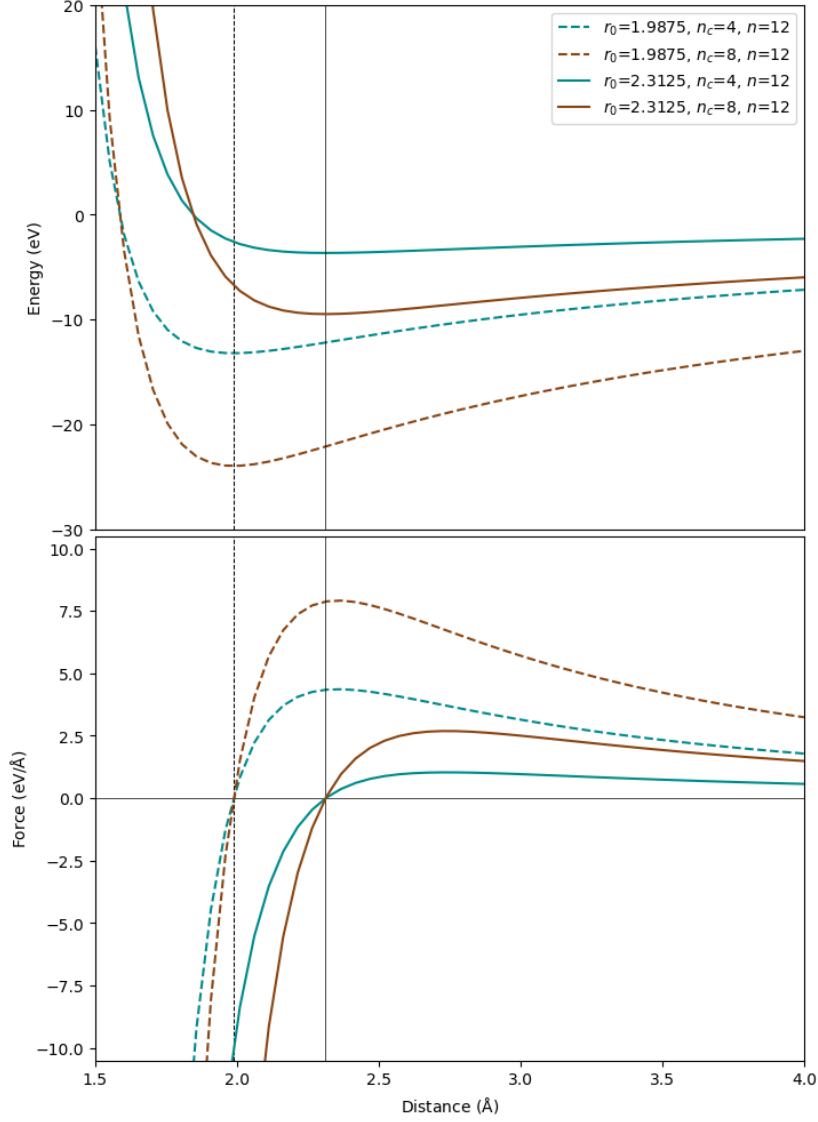


Figure 8: Energy and force from effective interatomic potentials for equilibrium bond lengths of 1.9875 and 2.3125 Å and coordination numbers of 4.0 and 8.0. All models have $n = 12$. These models are represented by the small filled and unfilled circles in Figure 4. ζ for these extreme models varies between 0.95 ($n_c = 8$ and $r_0 = 1.9875$) and 0.40 ($n_c = 4$ and $r_0 = 2.3125$).

545 This ionic model allows us to use the combination of empirical low pres-
546 sure measurement fractionation between olivine and coexisting melt at low
547 pressure together with the pressure evolution of the average structure of sil-
548 icate melts to calculate the reduced partition function for Mg in the melt
549 phase. To do this, we use the data of de Koker et al. (2009), shown in
550 Figure 7, to find the bond length and coordination number in the melt at
551 the pressure of interest, evaluate the effective force constant using the model
552 shown in Figure 4, and then use Equation 8 to compute the reduced partition
553 function for the melt at the temperature of interest. In order to ensure con-
554 sistency with the empirical result for fractionation between melt and olivine
555 we apply a constant offset (of 7.8 GPa) to the pressure scale. The resulting
556 predicted fractionation along a chondritic liquidus is shown in Figure 9 taking
557 the melt as the reference phase. The rapid increase in the mean Mg coor-
558 dination number in the melt as pressure increases from 0 to 25 GPa results
559 in a rapid increase in fractionation (i.e. more negative $\Delta^{26/24}\text{Mg}$) between
560 the solids and coexisting liquid. This trend then reverses as the coordina-
561 tion number of the melt stops increasing and the bond compressibility in the
562 melt dominates the modelled fractionation. Because the bond lengths in the
563 melt decrease in length more slowly than the bond lengths in the solids (as
564 added flexibility means the melt can decrease volume without a reduction
565 in bond length) $\Delta^{26/24}\text{Mg}$ between the solids and coexisting liquid begins to
566 increase but remains more extreme than the ambient pressure value. This
567 trend continues throughout the mantle pressure range. In principle these
568 patterns should impart an isotopic signature on the crystallising mantle that
569 could persist to today.

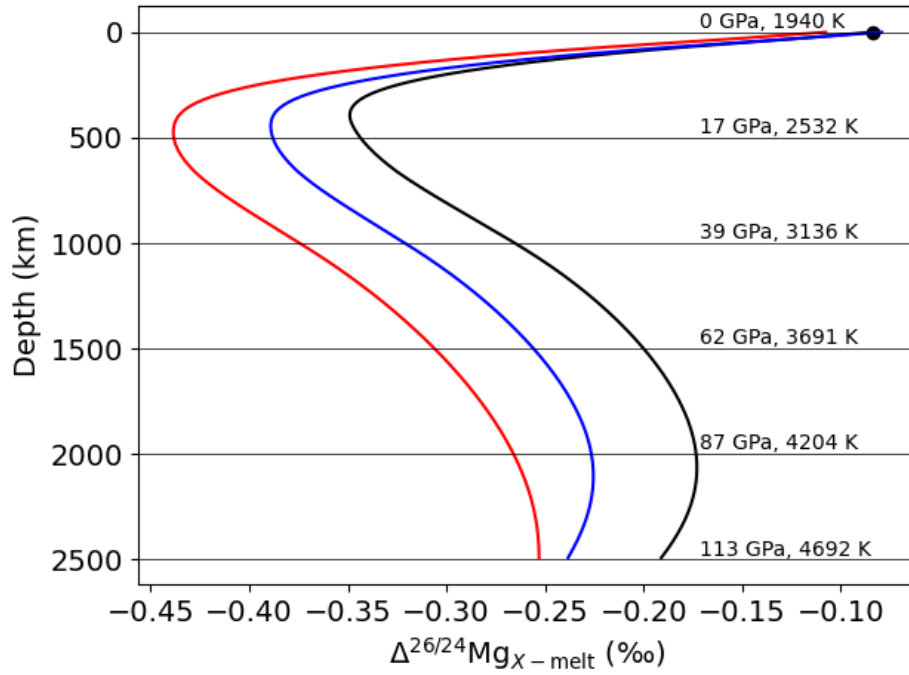


Figure 9: Calculated equilibrium partitioning between Fo (black lines), Bdm (red lines) or Per (blue lines) and melt as a function of depth along a chondritic liquidus. The black dot shows the observed fractionation between Fo and melt to which the model curves are pinned. The pressure and temperature of the chondritic liquidus at selected depths is indicated numerically towards the right hand side of the figure.. In this plot the reference liquid structure evolves with pressure and temperature.

570 Our principal aim is to explore Mg isotopic fractionations generated in
 571 the deep mantle as a result of a crystallising magma ocean (see following
 572 section). However, our calculations also have implications for the compo-
 573 sitions of modern mantle derived melts relative to their likely peridotitic
 574 sources. Notably, Figure 9 predicts that in the uppermost mantle, the $\delta^{26}\text{Mg}$
 575 of melts in equilibrium with olivine become markedly heavier with depth (i.e.
 576 $\Delta^{26/24}\text{Mg}_{\text{Fo-melt}}$ decreases until ~ 400 km). Common modern mantle melts
 577 are widely believed to be generated by melting of olivine-rich lithologies at
 578 depths up to ~ 150 km. Small degree melts of plumes upwelling beneath thick
 579 old lithosphere represent some of the melts produced at greatest depth. The
 580 values of $\Delta^{26/24}\text{Mg}_{\text{Fo-melt}}$ in Figure 9 suggest that such melts should have val-
 581 ues of $\delta^{26}\text{Mg}$ up to $\sim 0.25\%$ higher than an olivine dominated mantle source.
 582 Even shallower melts, such as mid-ocean ridge basalts (MORB, with mean
 583 melting depths ~ 30 km), should be have $\delta^{26}\text{Mg} \sim 0.15\%$ higher than mantle
 584 peridotites (i.e. $\Delta^{26/24}\text{Mg}_{\text{Fo-melt}} \sim -0.15\%$). Yet, most mantle derived melts
 585 have $\delta^{26}\text{Mg}$ similar to peridotites (e.g. Teng et al., 2010). This observation is
 586 already puzzling for calculations of melt $\delta^{26}\text{Mg}$ using the published ol-melt
 587 fractionation factor of Liu et al. (2022) that pins our parametrisation at 0
 588 GPa (see discussion in Soderman et al., 2024), but becomes more so using
 589 our extrapolations to higher pressure (Figure 9).

590 The role of diffusive fractionation during melt transport is a potential
 591 resolution of this problem. Recent analyses of MORB show a strong inverse
 592 correlation of $\delta^{26}\text{Mg}$ and $\delta^{57}\text{Fe}$, consistent with diffusive Mg-Fe exchange be-
 593 tween melts and melt-depleted mantle at the top of the melting column. This
 594 process should lower the $\delta^{26}\text{Mg}$ of erupted melts (Liu et al., 2024a). Further,

595 quantitative exploration is required to determine whether or not a decrease
596 in ^{26}Mg as large as $\sim 0.25\text{‰}$ is possible by diffusive interaction during trans-
597 port. However, current analysis argues that diffusive Mg-Fe exchange lowers
598 ^{26}Mg by at least 0.15‰ (Liu et al., 2024a) and so the influence of kinetic
599 fractionation in accounting for the unexpectedly low ^{26}Mg in modern melts
600 seems plausible.

601 It would be valuable to test the strong pressure dependence of $\Delta^{26/24}\text{Mg}_{\text{Fo-melt}}$
602 with petrological experiments, but this approach is made challenging by the
603 large isotopic fractionations imparted by Soret diffusion over temperature
604 gradients typical of high pressure experiments (Richter et al., 2008). This
605 problem has been documented specifically for Mg isotope ratio measurements
606 in a 1 GPa experimental charge (Liu et al., 2022). A more approachable test
607 of the robustness of our method of extrapolation of fractionation factors
608 with depth could be assessed by using atomic scale approaches to calculate
609 reduced partition coefficients for the melt phase using an averaged ensemble
610 of structures (Rabin et al., 2023).

Depth (km)	Pressure (GPa)	Temperature (K)	1000 ln(β)			
			Fo	Bdm	Per	melt
1000	39	3136	0.388	0.278	0.332	0.653
1500	62	3691	0.353	0.247	0.297	0.553
2000	87	4204	0.314	0.222	0.261	0.488
2500	113	4692	0.250	0.189	0.203	0.442

Table 6: Summary fractionation factors along a chondritic liquidus. Solids from DFPT with thermal expansion, liquid from an ionic model pinned to the empirical measurement at ambient pressure

611 *4.2. Implications for global magma oceans*

612 In the aftermath of a giant, moon-forming impact the Earth’s mantle was
613 largely molten (Benz and Cameron, 1990; Tonks and Melosh, 1993). From
614 either bottom-up (e.g. Solomatov and Stevenson, 1993) or middle-out crys-
615 tallisation scenarios (Labrosse et al., 2007), Bdm would be expected to be
616 the dominant crystallising phase (e.g. Ito et al., 2004). If any Bdm cumulate
617 reservoirs were preserved, they would have a significant impact on trace and
618 even major element abundances of the accessible mantle (e.g. Kato et al.,
619 1988). However, vigorous convection in both magma ocean and the subse-
620 quently crystallised mantle acts against such a reservoir persisting through
621 Earth history (e.g. Solomatov and Stevenson, 1993). Nonetheless, numer-
622 ous studies still invoke the chemical consequences of a primordial planetary
623 magma ocean in shaping modern mantle compositions (see discussion in Wal-
624 ter and Trønnes, 2004). The signature of Bdm fractionation has also been
625 inferred in the sources of some Archean magmas, from their ‘decoupled’ Sm-
626 Nd and Lu-Hf systematics (e.g. Hoffmann et al., 2011; Rizo et al., 2011;
627 Puchtel et al., 2013; Boyet et al., 2021) and in one case this has been further
628 linked to Fe isotopic fractionation (Williams et al., 2021). The significant
629 Mg isotopic fractionation between Bdm and melt that we have quantified
630 for lower mantle pressures provides a useful means to test some of these
631 scenarios.

632 As a moderately refractory element, the Mg isotopic compositions of chon-
633 dritic meteorites give a valuable estimate of bulk Earth and in turn bulk sili-
634 cate Earth, given Mg is highly lithophile and minimally incorporated into the
635 core. Recent, critical mixture double spiking analyses have helped refine the

636 composition of chondrites (Hin et al., 2017) and the accessible upper mantle
637 (Liu et al., 2023). These new data show that the Earth’s accessible mantle
638 is slightly isotopically heavier than the likely dominant chondritic starting
639 materials by some 12-38 ppm in $\Delta^{26/24}\text{Mg}$, assuming enstatite chondrite type
640 protolith based on its isotopic similarity to Earth (e.g. Dauphas, 2017). Al-
641 though the difference in $\Delta^{26/24}\text{Mg}$ between (enstatite) chondrite and Earth
642 was previously explained by evaporative loss during accretion (Hin et al.,
643 2017), the sense of fractionation is also compatible with loss of Bdm from
644 the accessible mantle, a concept which has been the focus of some renewed
645 attention (see review in Murakami et al., 2024). Here we explore this latter
646 possibility more quantitatively using our new fractionation factors.

647 We consider a simple batch model of magma ocean crystallisation, as it
648 has been argued that the vigour of convective mixing in the magma ocean
649 makes fractional removal of solid phases unlikely until at least 50% crys-
650 tallisation (Solomatov and Stevenson, 1993). The consequences of increasing
651 amounts of solid Bdm removal from a global magma ocean are illustrated
652 on Figure 10. Loss of isotopically light Bdm from the magma ocean in-
653 creases the $^{26}\text{Mg}/^{24}\text{Mg}$ of the residual melt (red lines, Figure 10) relative to
654 its initial, chondritic composition. If some proportion of the crystallised Bdm
655 remains isolated through Earth history, due to its higher viscosity for exam-
656 ple (Ballmer et al., 2017), then the convectively stirred, accessible mantle
657 will acquire the Mg isotopic composition of the (subsequently crystallised)
658 evolved liquid shown in Figure 10.

659 We use fractionation factors for $^{26}\text{Mg}/^{24}\text{Mg}$ between Bdm and melt at
660 two different depths: at 2500 km appropriate for crystallisation at the base

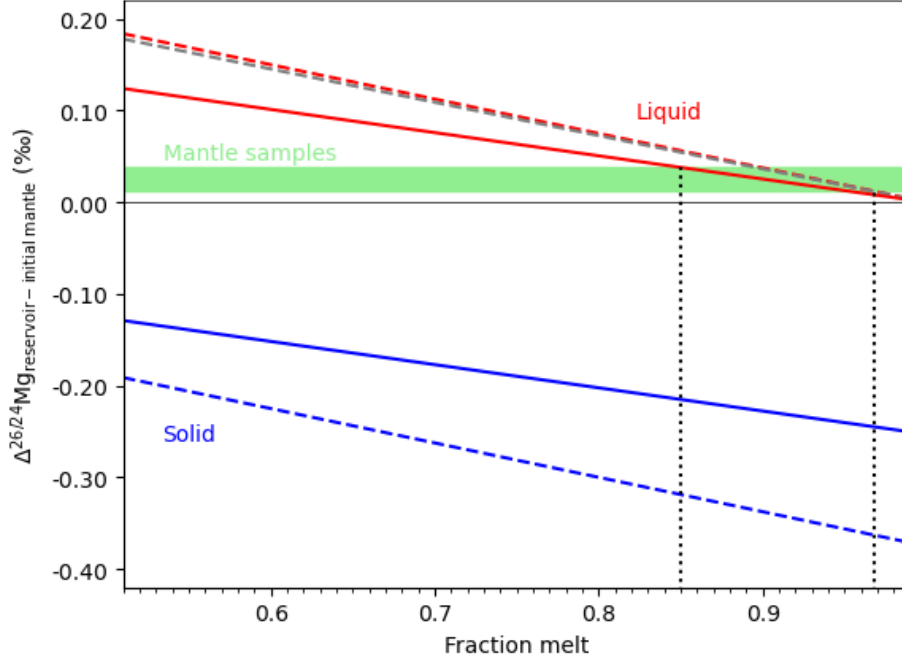


Figure 10: Difference in $^{26}\text{Mg}/^{24}\text{Mg}$ relative to an initial (chondritic) composition ($\Delta^{26/24}\text{Mg}$, expressed in ‰) of evolving melt (red lines) and solid (blue lines) during magma ocean crystallisation. We consider the first 50% crystallisation (i.e. melt fraction, by mass, decreases from 1 to 0.5) in which interval crystallisation is likely a batch process (Solomatov and Stevenson, 1993) and Bdm the dominant crystallising phase (Ito et al., 2004). The effect of also including 10 wt.% Per fractionation with the Bdm has a minor effect (shown as grey dashed line compared to red dashed line). Scenarios using two different fractionation factors, temperatures, and pressures from Table 6 are shown: the solid lines for deep mantle crystallisation (2500 km) and dashed lines for mid mantle crystallisation (1000 km). The green box indicates the range of composition of the samples from the Earth’s mantle (Liu et al., 2023) relative to an enstatite chondrite starting composition (Hin et al., 2017). Depending on the fractionation scenario, 3-15 wt.% Bdm fractionation (and subsequent isolation, indicated by the vertical black dotted lines) is sufficient to explain the super-chondritic $^{26}\text{Mg}/^{24}\text{Mg}$ of the Earth’s mantle.

661 of a magma ocean and at 1000 km to represent mid-mantle crystallisation
662 (Caracas et al., 2019) with physical conditions and reduced partition func-
663 tions reported in Table 6. These two values should span the range of crys-
664 tallisation scenarios and the outcomes are shown as solid and dashed lines
665 respectively in Figure 10. We assume pure Bdm fractionation, which is likely
666 the case for up to 50% crystallisation of the magma ocean, although the ad-
667 ditional contribution of Per to the crystallisation assemblage, which is also
668 isotopically light relative to melt in the lower mantle (Table 6), does not
669 significantly change the calculations (Figure 10).

670 The Mg isotopic composition of the terrestrial mantle relative to enstatite
671 chondrites (and the uncertainty on this value) is shown as a green box on Fig-
672 ure 10. In order to reproduce such $\Delta^{26/24}\text{Mg}$ requires a minimum of 3 wt.%
673 and maximum of 15 wt.% Bdm crystallisation and its subsequent convective
674 isolation. This range of Bdm fractionation is similar to that suggested by
675 Walter and Trønnes (2004) as being compatible with a range of refractory
676 element ratios in silicate Earth. We note that the latter estimates also re-
677 quire minor davemaoite crystallisation to counter-act some the more extreme
678 trace element fractionations of Bdm on key trace element ratios, whereas our
679 estimate is not sensitive to this additional consideration. The amount of
680 convectively isolated Bdm required to satisfy the Mg isotope constraints is
681 also consistent with the geodynamical simulations of Gülcher et al. (2020).

682 While these calculations might suggest a hidden, cumulate Bdm reservoir
683 is a plausible solution to the accessible Earth having superchondritic man-
684 tle $^{26}\text{Mg}/^{24}\text{Mg}$, the longevity of stiff Bdm domains in the mantle still needs
685 to be fully explored in 3-dimensional simulations. Moreover there are ad-

ditional considerations from mass dependent Si isotope measurements. The Moon and accessible terrestrial mantle are indistinguishable in their $\Delta^{30/28}\text{Si}$ (Fitoussi and Bourdon, 2012; Zambardi et al., 2013; Armytage et al., 2011). Fitoussi and Bourdon (2012) argued that this left little scope for a hidden Bdm reservoir on Earth, given Bdm is also anticipated to fractionate Si as well as Mg isotopes at magma ocean conditions (Huang et al., 2014). Given our progress in providing melt-Bdm fractionation factors, extending this approach to Si, to couple with new critically mixed double spike measurements (Liu et al., 2024b), would be valuable to address this issue in new detail.

5. Conclusions

We have made first principles calculations of Mg isotope fractionation between the major Mg-bearing phases of the lower mantle from the transition zone (25 GPa) to core mantle boundary (120 GPa). For temperatures on a chondritic liquidus (3200-4700 K), and including the effects of thermal expansion, fractionations of $^{26}\text{Mg}/^{24}\text{Mg}$ between Per, Bdm and a fictive Fo reference vary from 0.056 to 0.047‰ and 0.11 to 0.061‰, respectively. Thus, we reconfirm that diminished isotopic fractionation resulting from higher temperatures deeper in the Earth is sufficiently compensated by the effects of pressure to permit discernible Mg isotopic fractionations under lower mantle conditions.

We have also made an initial estimate of the isotopic fractionation between the solid lower mantle phases and co-existing melt. We first calculated the $1000\ln \beta$ for a set of MgO-structured minerals with different Mg coordination number and Mg-O bond length, to allow us to parameterise the effects of

710 these two controls on isotopic fractionation. We then used data from ab ini-
711 tio models of melt structure to characterise Mg coordination and Mg-O bond
712 length in silicate melts with changing pressure. The model was then pinned
713 to an empirical determination of $^{26}\text{Mg}/^{24}\text{Mg}$ fractionation between Fo and
714 melt at 0 GPa. Using this approach, we predict $\Delta^{26/24}\text{Mg}_{\text{Bdm-melt}} = -0.38$ to
715 -0.25‰ from the transition zone to core mantle boundary for temperatures
716 on a chondritic liquidus. Using this quantification of the influence of melt
717 structure on Mg isotopic fractionation we show that the high coordination
718 number Mg site in Bdm leads to discernible Mg isotopic fractionation during
719 its crystallisation from a magma ocean.

720 Using these fractionation factors in combination with $^{26}\text{Mg}/^{24}\text{Mg}$ mea-
721 surements made to a precision of <20 ppm can provide useful constraints
722 on scenarios of magma ocean crystallisation. This approach rules out hid-
723 den, primordial cumulate reservoirs greater than 15 wt.% of the mantle but
724 suggests that the slightly super-chondritic $^{26}\text{Mg}/^{24}\text{Mg}$ of the Earth could be
725 explained by removal of 3-15% Bdm during magma ocean crystallisation,
726 if primordial cumulate Bdm can be retained, unmixed with the rest of the
727 mantle over Earth history, as hypothesised in the BEAMS concept of Ballmer
728 et al. (2017). The strength of this explanation relative to a previous proposal
729 of evaporative loss (Hin et al., 2017) could usefully be tested with a similar
730 quantification of deep mantle Si isotope fractionation.

731 Acknowledgments

732 We acknowledge the use of HECToR, ARCHER and ARCHER2 the UK's
733 national high-performance computing services. We thank the two anonymous

734 reviewers of a 2014 version of this manuscript who provided some useful
735 suggestions and four reviewers of this manuscript for their reviews. This work
736 is supported by grants from NERC (NE/L007428/1 and NE/K008803/1) and
737 the ERC (NONUNE, 885531 and VapLoss, 949417). For the purpose of Open
738 Access, the authors have applied a CC BY public copyright licence to any
739 Author Accepted Manuscript (AAM) version arising from this submission.

740 **Data Availability**

741 Density functional theory calculations were performed using the CASTEP
742 code with code available via <https://www.castep.org/>. Input and output files
743 for these calculations are available through Zenodo at <https://doi.org/10.5281/zenodo.16760721>.
744 Software used to calculate and fit reduced partition functions, and create all
745 figures presented in this manuscript, is also available through Zenodo at
746 <https://doi.org/10.5281/zenodo.16744738>.

747 **Appendix A. Supplementary Material**

748 The supplementary file describes our parametrisation of reduced partition
749 functions for crystals and melt with pressure, temperature and depth. It also
750 includes tables of the fitted coefficients used for this alongside an expanded
751 version of Table 6.

References

Andrault, D., Bolfan-Casanova, N., Lo Nigro, G., Bouhifd, M.A., 2011.
Solidus and liquidus profiles of chondritic mantle: Implication for melt-

- ing of the earth across its history. *Earth and Planetary Science Letters* 304, 251 – 259. doi:10.1016/j.epsl.2011.02.006.
- Armytage, R.M.G., Georg, R.B., Savage, P.S., Williams, H.M., Halliday, A.N., 2011. Silicon isotopes in meteorites and planetary core formation. *Geochimica et Cosmochimica Acta* 75, 3662 – 3676. doi:10.1016/j.gca.2011.03.044.
- Ballmer, M.D., Houser, C., Hernlund, J.W., Wentzcovitch, R.M., Hirose, K., 2017. Persistence of strong silica-enriched domains in the Earth's lower mantle. *Nature Geoscience* 10, 236–240. doi:10.1038/ngeo2898.
- Baroni, S., Giannozzi, P., Testa, A., 1987. Green's-function approach to linear response in solids. *Physical Review Letters* 58, 1861 – 1864.
- Baroni, S., de Gironcoli, S., Corso, A.D., Giannozzi, P., 2001. Phonons and related crystal properties from density-functional perturbation theory. *Reviews of Modern Physics* 73, 515 – 562.
- Benz, W., Cameron, A.G.W., 1990. Terrestrial Effects Of The Giant Impact, in: *Origin of the Earth*. Oxford University Press New York, NY, pp. 61–67. URL: <https://academic.oup.com/book/53843/chapter/422184126>, doi:10.1093/oso/9780195066197.003.0005.
- Bigeleisen, J., Mayer, M.G., 1947. Calculation of equilibrium constants for isotopic exchange reactions. *Journal of Chemical Physics* 15, 261 – 267. doi:10.1063/1.1746492.
- Blanchard, M., Balan, E., Schauble, E.A., 2017. Equilibrium fractionation

- of non-traditional isotopes: a molecular modeling perspective. *Reviews in Mineralogy and Geochemistry* 82, 27–63. doi:10.2138/rmg.2017.82.2.
- Blanchard, M., Poitrasson, F., Méheut, M., Lazzeri, M., Mauri, F., Balan, E., 2009. Iron isotope fractionation between pyrite (FeS_2), hematite (Fe_2O_3) and siderite (FeCO_3): A first-principles density functional theory study. *Geochimica et Cosmochimica Acta* 73, 6565 – 6578.
- Boyet, M., Garçon, M., Arndt, N., Carlson, R., Konc, Z., 2021. Residual liquid from deep magma ocean crystallization in the source of komatiites from the ICDP drill core in the Barberton Greenstone Belt. *Geochimica et Cosmochimica Acta* 304, 141–159.
- Caracas, R., Hirose, K., Nomura, R., Ballmer, M.J., 2019. Melt–crystal density crossover in a deep magma ocean. *Earth and Planetary Science Letters* 516, 202–211. doi:10.1016/j.epsl.2019.03.031.
- Clark, S.J., Segall, M.D., Pickard, C.J., Hasnip, P.J., Probert, M.I.J., Refson, K., Payne, M.C., 2005. First principles methods using CASTEP. *Zeitschrift fuer Kristallographie* 220, 567 – 570.
- Dauphas, N., 2017. The isotopic nature of the earth’s accreting material through time. *Nature* 541, 521–524. doi:10.1038/nature20830.
- Duan, H., Yang, B., Huang, F., 2023. Site-specific isotope effect: Insights from equilibrium magnesium isotope fractionation in mantle minerals. *Geochimica et Cosmochimica Acta* 357, 13–25. doi:10.1016/j.gca.2023.05.015.

- Fitoussi, C., Bourdon, B., 2012. Silicon isotope evidence against an enstatite chondrite Earth. *Science* 335, 1477 – 1480. doi:10.1126/science.1219509.
- Gao, C., Cao, X., Liu, Q., Yang, Y., Zhang, S., He, Y., Tang, M., Liu, Y., 2018. Theoretical calculation of equilibrium mg isotope fractionations between minerals and aqueous solutions. *Chemical Geology* 488, 62–75. doi:10.1016/j.chemgeo.2018.04.005.
- Giannozzi, P., de Gironcoli, S., Pavone, P., Baroni, S., 1991. *Ab initio* calculation of phonon dispersion in semiconductors. *Physical Review B* 43, 7231 – 7242.
- Gonze, X., 1997. First-principles responses of solids to atomic displacements and homogeneous electric fields: Implementation of a conjugate-gradient algorithm. *Physical Review B* 55, 10337 – 10354.
- Gonze, X., Lee, C., 1997. Dynamical matrices, Born effective charges, dielectric permittivity tensors, and interatomic force constants from density-functional perturbation theory. *Physical Review B* 55, 10355 – 10368.
- Gülcher, A.J.P., Gebhardt, D.J., Ballmer, M.J., Tackley, P.J., 2020. Variable dynamic styles of primordial heterogeneity preservation in the earth’s lower mantle. *Earth and Planetary Science Letters* 536, 116160. doi:10.1016/j.epsl.2020.116160.
- Hin, R.C., Coath, C.D., Carter, P.J., Nimmo, F., Lai, Y.J., Pogge Von Strandmann, P.A.E., Willbold, M., Leinhardt, Z.M., Walter, M.J., Elliott, T., 2017. Magnesium isotope evidence that accretional vapour loss shapes planetary compositions. *Nature* 549, 511–515. doi:10.1038/nature23899.

- Hoffmann, J.E., Münker, C., Polat, A., Rosing, M.T., Schulz, T., 2011. The origin of decoupled Hf—Nd isotope compositions in Eoarchean rocks from southern West Greenland. *Geochimica et Cosmochimica Acta* , 6610 – 6628doi:10.1016/j.gca.2011.08.018.
- Hohenberg, P., Kohn, W., 1964. Inhomogeneous electron gas. *Physical Review* 136, 864 – 871.
- Huang, F., Chen, L., Wu, Z., Wang, W., 2013. First-principles calculations of equilibrium Mg isotope fractionations between garnet, clinopyroxene, orthopyroxene, and olivine: Implications for Mg isotope thermometry. *Earth and Planetary Science Letters* 367, 61 – 70. doi:10.1016/j.epsl.2013.02.025.
- Huang, F., Wu, Z., Huang, S., Wu, F., 2014. First-principles calculations of equilibrium silicon isotope fractionation among mantle minerals. *Geochimica et Cosmochimica Acta* 140, 509 – 520. doi:10.1016/j.gca.2014.05.035.
- Ito, E., Kubo, A., Katsura, T., Walker, M.J., 2004. Melting experiments of mantle materials under lower mantle conditions with implications for magma ocean differentiation. *Physics of the Earth and Planetary Interiors* 143-144, 397–406. doi:10.1016/j.pepi.2003.09.016.
- Javoy, M., Balan, E., Méheut, M., Blanchard, M., Lazzeri, M., 2012. First-principles investigation of equilibrium isotopic fractionation of O- and Si-isotopes between refractory solids and gases in the solar nebula. *Earth and Planetary Science Letters* 319-320, 118 – 127. doi:10.1016/j.epsl.2011.12.029.

- Karki, B.B., Bhattarai, D., Stixrude, L., 2006. First-principles calculations of the structural, dynamical, and electronic properties of liquid MgO. *Physical Review B* 73, art. num. 174208. doi:10.1103/PhysRevB.73.174208.
- Kato, T., Ringwood, A.E., Irifune, T., 1988. Experimental determination of element partitioning between silicate perovskites, garnets and liquids: constraints on early differentiation of the mantle. *Earth and Planetary Science Letters* 89, 123–145. doi:10.1016/0012-821x(88)90038-6.
- Keiffer, S.W., 1982. Thermodynamics and lattice vibrations of minerals: 5. applications to phase equilibria, isotopic fractionation, and high-pressure thermodynamic properties. *Reviews of Geophysics and Space Physics* 20, 827 – 849.
- Kohn, W., Sham, L.J., 1965. Self-consistent equations including exchange and correlation effects. *Physical Review* 140, 1133 – 1138.
- de Koker, N., 2009. Thermal conductivity of MgO periclase from equilibrium first principles molecular dynamics. *Physical Review Letters* 103, 125902. doi:10.1103/PhysRevLett.103.125902.
- de Koker, N.P., Stixrude, L., Karki, B.B., 2009. Thermodynamics, structure, dynamics, and freezing of Mg₂SiO₄ liquid at high pressure. *Geochimica et Cosmochimica Acta* 72, 1427 – 1441.
- Kowalski, P.M., Jahn, S., 2011. Prediction of equilibrium Li isotope fractionation between minerals and aqueous solutions at high P and T : An efficient *ab initio* approach. *Geochimica et Cosmochimica Acta* 75, 6112 – 6123. doi:10.1016/j.gca.2011.07.039.

- Kowalski, P.M., Wunder, B., Jahn, S., 2013. *Ab initio* prediction of equilibrium boron isotope fractionation between minerals and aqueous fluids at high P and T . *Geochimica et Cosmochimica Acta* 101, 285 – 301. doi:dx.doi.org/10.1016/j.gca.2012.10.007.
- Labrosse, S., Hernlund, J.W., Coltice, N., 2007. A crystallizing dense magma ocean at the base of the Earth's mantle. *Nature* 450, 866 – 869. doi:10.1038/nature06355.
- Li, X., Liu, Y., 2011. Equilibrium Se isotope fractionation parameters: A first-principles study. *Earth and Planetary Science Letters* 304, 113 – 120. doi:10.1016/j.epsl.2011.01.022.
- Li, X., Zho, H., Tang, M., Liu, Y., 2009. Theoretical prediction for several important equilibrium Ge isotope fractionation factors and geological implications. *Earth and Planetary Science Letters* 287, 1 – 11. doi:10.1016/j.epsl.2009.07.027.
- Liu, X.N., Hin, R., Coath, C., van Soest, M., Melekhova, E., Elliott, T., 2022. Equilibrium olivine-melt Mg isotopic fractionation explains high $\delta^{26}\text{Mg}$ values in arc lavas. *Geochemical Perspectives Letters* 22, 42–47. doi:10.7185/geochemlet.2226.
- Liu, X.N., Hin, R.C., Coath, C.D., Bizimis, M., Su, L., Ionov, D.A., Brooker, R., Elliott, T., 2023. The magnesium isotopic composition of the mantle. *Geochimica et Cosmochimica Acta* 358, 12–26. doi:10.1016/j.gca.2023.08.011.

- Liu, X.N., Hin, R.C., Coath, C.D., Elliott, T., 2024a. Mg and Fe isotope compositions of mid-ocean ridge basalts modified by Mg-Fe inter-diffusion during melt transport. *Earth and Planetary Science Letters* 642, 118868. doi:10.1016/j.epsl.2024.118868.
- Liu, X.N., Klava, M., Hin, R.C., Coath, C.D., Ng, H.C., Elliott, T., 2024b. High-precision, mass dependent si isotope measurements *via* the critical mixture double-spiking technique. *Journal of Analytical Atomic Spectrometry* 39, 2799–2808. doi:10.1039/d4ja00152d.
- Méheut, M., Lazzeri, M., Balan, E., Mauri, F., 2007. Equilibrium isotopic fractionation in the kaolinite, quartz, water system: Prediction from first-principles density-functional theory. *Geochimica et Cosmochimica Acta* 71, 3170 – 3181. doi:10.1016/j.gca.2007.04.012.
- Méheut, M., Lazzeri, M., Balan, E., Mauri, F., 2009. Structural control over equilibrium silicon and oxygen isotopic fractionation: A first-principles density-functional theory study. *Chemical Geology* 258, 28 – 37. doi:10.1016/j.chemgeo.2008.06.051.
- Monkhorst, H.J., Pack, J.D., 1976. Special points for Brillouin-zone integrations. *Physical Review B* 13, 5188 – 5192.
- Mookherjee, M., Stixrude, L., Karki, B., 2008. Hydrous silicate melt at high pressure. *Nature* 452, 983 – 986.
- Murakami, M., Kahn, A., Sossi, P.A., Ballmer, M.D., Saha, P., 2024. The composition of Earth’s lower mantle. *Annual Review of Earth and Planetary Sciences* 52, 605–638. doi:10.1146/annurev-earth-031621-075657.

- Payne, M.C., Teter, M.P., Allan, D.C., Arias, T., Joannopoulos, J.D., 1992. Iterative minimization techniques for *ab initio* total-energy calculations: molecular-dynamics and conjugate gradients. *Reviews of Modern Physics* 64, 1045 – 1067.
- Perdew, J.P., Burke, K., Ernzerhof, M., 1996. Generalized gradient approximation made simple. *Physical Review Letters* 77, 3865 – 3868.
- Puchtel, I., Blichert-Toft, J., Touboul, M., Walker, R., Byerly, G., Nisbet, E., Anhaeusser, C., 2013. Insights into early Earth from Barberton komatiites: evidence from lithophile isotope and trace element systematics. *Geochimica et Cosmochimica Acta* 108, 63–90.
- Rabin, S., Blanchard, M., Pinilla, C., Poitrasson, F., Grégoire, M., 2023. Iron and silicon isotope fractionation in silicate melts using first-principles molecular dynamics. *Geochimica et Cosmochimica Acta* 343, 212–233. doi:10.1016/j.gca.2022.11.017.
- Refson, K., Tulip, P.R., Clark, S.J., 2006. Variational density-functional perturbation theory for dielectrics and lattice dynamics. *Physical Review B* 73, 155114. doi:10.1103/PhysRevB.73.155114.
- Richter, F.M., Watson, E.B., Mendybaev, R.A., Teng, F.Z., Janney, P.E., 2008. Magnesium isotope fractionation in silicate melts by chemical and thermal diffusion. *Geochimica et Cosmochimica Acta* 72, 206–220.
- Rizo, H., Boyet, M., Blichert-Toft, J., Rosing, M., 2011. Combined Nd and Hf isotope evidence fro deep-seated source of Isua lavas. *Earth and Planetary Science Letters* 312, 267 – 279. doi:10.1016/j.epsl.2011.10.014.

- Rustad, J.R., Bylaska, E.J., 2006. Ab initio calculation of isotopic fractionation in $\text{B}(\text{OH})_3(\text{aq})$ and $\text{BOH}_4^-(\text{aq})$. *Journal of the American Chemical Society (communications)* 129, 2222 – 2223.
- Rustad, J.R., Dixon, D.A., 2009. Prediction of iron-isotope fractionation between hematite ($\alpha\text{-Fe}_2\text{O}_3$) and ferric and ferrous iron in aqueous solution from density functional theory. *Journal of Physical Chemistry A* 113, 12249 – 12255. doi:10.1021/jp9065373.
- Schauble, E.A., 2004. Applying stable isotope fractionation theory to new systems. *Reviews in Mineralogy and Geochemistry* 55, 65 – 111.
- Schauble, E.A., 2011. First-principles estimates of equilibrium magnesium isotope fractionation in silicate, oxide, carbonate and hexaaquamagnesium(2+) crystals. *Geochimica et Cosmochimica Acta* 75, 844 – 869. doi:10.1016/j.gca.2010.09.044.
- Soderman, C.R., Matthews, S., Shorttle, O., Jackson, M.G., Day, J.M.D., Kamenetsky, V., Williams, H.M., 2024. Global oceanic basalt sources and processes viewed through combined Fe and Mg stable isotopes. *Earth and Planetary Science Letters* 638, 118749. doi:10.1016/j.epsl.2024.118749.
- Soderman, C.R., Shorttle, O., Matthews, S., M., W.H., 2022. Global trends in novel stable isotopes in basalts: Theory and observations. *Geochimica et Cosmochimica Acta* 318, 388–414. doi:10.1016/j.gca.2021.12.008.
- Solomatov, V.S., Stevenson, D.J., 1993. Nonfractional crystallization of a terrestrial magma ocean. *Journal of Geophysical Research* 98, 5391 – 5406.

- Sossi, P.A., O'Neill, H.St.C., 2017. The effect of bonding environment on iron isotope fractionation between minerals at high temperature. *Geochimica et Cosmochimica Acta* 196, 121–143. doi:10.1016/j.gca.2016.09.017.
- Stixrude, L., Karki, B.B., 2005. Structure and freezing of MgSiO₃ liquid in Earth's lower mantle. *Science* 310, 297 – 299. doi:10.1126/science.1116952.
- Sun, N., Stixrude, L., de Koker, N., Karki, B.B., 2011. First principles molecular dynamics simulations of diopside (CaMgSi₂O₆) liquid to high pressure. *Geochimica et Cosmochimica Acta* 75, 3792 – 3802.
- Teng, F.Z., Li, W.Y., Ke, S., Marty, B., Dauphas, N., Huang, S.C., Wu, F.Y., Pourmand, A., 2010. Magnesium isotopic composition of the earth and chondrites. *Geochimica et Cosmochimica Acta* 74, 4150 – 4166. doi:10.1016/j.gca.2010.04.019.
- Teng, F.Z., Wadhwa, M., Helz, R.T., 2007. Investigation of magnesium isotope fractionation during basalt differentiation: implications for a chondritic composition of the terrestrial mantle. *Earth and Planetary Science Letters* 261, 84 – 92.
- Tonks, W.B., Melosh, H.J., 1993. Magma ocean formation due to giant impacts. *Journal of Geophysical Research* 98, 5319 – 5333. doi:10.1029/92JE02726.
- Urey, H.C., 1947. The thermodynamic properties of isotopic substances. *Journal of the Chemical Society* , 562 – 581doi:10.1039/JR9470000562.
- Walter, M.J., Trønnes, R.G., 2004. Early Earth differentiation. *Earth and Planetary Science Letters* 225, 253–269. doi:10.1016/j.epsl.2004.07.008.

- Wang, W., Tian, Q., Chen, Z., Huang, S., Wu, Z., Huang, F., 2017. Concentration effect on equilibrium fractionation of Mg-Ca isotopes in carbonate minerals: Insights from first-principles calculations. *Geochimica et Cosmochimica Acta* 208, 185–197. doi:10.1016/j.gca.2017.03.023.
- Wang, W., Wu, Z., Huang, S., Huang, F., 2023. First-principles investigation of equilibrium magnesium isotope fractionation among mantle minerals: Review and new data. *Earth-Science Reviews* 237, 104315. doi:10.1016/j.earscirev.2023.104315.
- Wang, W., Zhou, C., Liu, Y., Wu, Z., Huang, F., 2019. Equilibrium Mg isotope fractionation among aqueous Mg^{2+} , carbonates, brucite and lizardite: Insights from first-principles molecular dynamics simulations. *Geochimica et Cosmochimica Acta* 250, 117–129. doi:10.1016/j.gca.2019.01.042.
- Wentzcovitch, R.M., Yu, Y.G., Wu, Z., 2010. Thermodynamic properties and phase relations in mantle minerals investigated by first principles quasiharmonic theory, in: Wentzcovitch, R.M., Stixrude, L. (Eds.), *Theoretical and computational methods in mineral physics: geophysical applications*. Mineralogical society of America and the Geochemical Society. volume 71 of *Reviews in Mineralogy and Geochemistry*. chapter 4, pp. 59 – 98.
- Williams, H.M., Matthews, S., Rizo, H., Shorttle, O., 2021. Iron isotopes trace primordial magma ocean cumulates melting in Earth’s upper mantle. *Science Advances* 7, eabc7394. doi:10.1126/sciadv.abc7394.
- Wu, Z., Huang, F., Huang, S., 2015. Isotope fractionation induced by phase

- transformation: First-principles investigation for Mg_2SiO_4 . *Earth and Planetary Science Letters* 409, 339 – 347. doi:10.1016/j.epsl.2014.11.004.
- Xiao, Z.C., Zhou, C., Kang, J.T., Z.-Q., W., Huang, F., 2022. The factors controlling equilibrium inter-mineral Ca isotope fractionation: Insights from first-principles calculations. *Geochimica et Cosmochimica Acta* 333, 373–389. doi:10.1016/j.gca.2022.07.021.
- Yagi, T., Mao, H.K., Bell, P.M., 1978. Structure and crystal chemistry of perovskite-type MgSiO_3 . *Physics and Chemistry of Minerals* 3, 97 – 110. doi:10.1007/BF00308114.
- Young, E.D., Manning, C.E., Schauble, E.A., Shahar, A., Macris, C.A., 2015. High-temperature equilibrium isotope fractionation of non-traditional stable isotopes: Experiments, theory, and applications. *Chemical Geology* 395, 176 – 195. doi:10.1016/j.chemgeo.2014.12.013.
- Young, E.D., Tonui, E., Manning, C.E., Schauble, E., Macris, C.A., 2009. Spinel–olivine magnesium isotope thermometry in the mantle and implications for the Mg isotopic composition of Earth. *Earth and Planetary Science Letters* 288, 524 – 533. doi:10.1016/j.epsl.2009.10.014.
- Zambardi, T., Poitrasson, F., Corgne, A., Méheut, M., Quitté, G., Anand, M., 2013. Silicon isotope variations in the inner solar system: Implications for planetary formation, differentiation and composition. *Geochimica et Cosmochimica Acta* 121, 67–83. doi:10.1016/j.gca.2013.06.040.

Supplementary information for: Controls on Mg isotopic fractionation between deep mantle phases and relict signatures of a terrestrial magma ocean

Andrew M. Walker

Department of Earth Sciences, University of Oxford, South Parks Road, Oxford, OX1 3AN, UK.

Remco C. Hin

Institute of Environmental Geology and Geoengineering, CISA Nazionale delle Ricerche, Via Mario Bianco 9, 20131, Milano MI, Italy.

Tim Elliott

School of Earth Sciences, University of Bristol, Queen's Road, Bristol, BS8 1RT, UK.

1 Parametrisation of magnesium fractionation in crystals as a function of depth

In Figure 6 in the main text we present results of the fractionation of magnesium isotopes between forsterite and MgO, and forsterite and bridgmanite as a function of depth along a geotherm for two cases. In the first (shown with dashed lines) we neglect the thermal expansion of the three phases. The parametrisation for this case is fairly compact and given by Equation 5 and Table 3 in the main text. The second case (shown as a solid line in Figure 6) includes the differential thermal expansion of the phases as calculated using lattice dynamics in the quasi-harmonic approximation. While probably more accurate, the parametrisation for this case demands many more terms. Here we outline the steps we use to generate the data in Figure 6, and list the full set of parameters to allow our results to be reused.

It is first worth noting that we are interested in calculating the isotopic fractionation along the chondritic melting curve of [Andrault et al. \(2011\)](#) which, for any depth, defines the temperature, T , and pressure, P , where we will evaluate the fractionation. However, the reduced partition functions are calculated as a function of unit cell volume, V , and

T . The first stage is thus to find V for the relevant P and T . To do this, we first calculate the Helmholtz free energy, F , as a function of T for unit cells of fixed structure and hence fixed V . The structures are found by static minimisation of the enthalpy for 16 applied pressures between -10 and 140 GPa in 10 GPa increments. Results for each T are fit to isothermal third-order Birch-Murnaghan equations of state:

$$F(V) = F_0 + \frac{9V_0K_0}{16} \left\{ \left[\left(\frac{V_0}{V} \right)^{\frac{2}{3}} - 1 \right]^3 K'_0 + \left[\left(\frac{V_0}{V} \right)^{\frac{2}{3}} - 1 \right]^2 \left[6 - 4 \left(\frac{V_0}{V} \right)^{\frac{2}{3}} \right] \right\}. \quad (1)$$

In order to find the volume at any temperature and pressure, we fit the four parameters, X , of these equations (the zero pressure Helmholtz free energy, F_0 , the zero pressure volume, V_0 , the zero pressure bulk modulus, K_0 , and its pressure derivative K'_0) to fifth order polynomials in T :

$$X(T) = X_5T^5 + X_4T^4 + X_3T^3 + X_2T^2 + X_1T + X_0, \quad (2)$$

and this allows us to easily find the parameters for any temperature, which allows us to evaluate the pressure as a function of volume at that temperature from the derivative of Equation 1:

$$P(V) = \frac{3K_0}{2} \left[\left(\frac{V_0}{V} \right)^{\frac{7}{3}} - \left(\frac{V_0}{V} \right)^{\frac{5}{3}} \right] \left\{ 1 + \frac{3}{4}(K'_0 - 4) \left[\left(\frac{V_0}{V} \right)^{\frac{2}{3}} - 1 \right] \right\}. \quad (3)$$

Coefficients of Equation 2 are given in Table 1. The results are also shown in Figure 5 of the main text. Equation 3 is not invertible, so to find volume as a function of pressure we resort to a numerical approach and perform a bisection search (using SciPy; Virtanen et al., 2020) to find the volume for which Equation 3 returns the desired pressure (for parameters which depend on temperature using Equation 2).

The reduced partition functions are similarly calculated as a function of unit cell volume and temperature for the same set of cell volumes. To allow interpolation to other temperatures or cell volumes these results are fit to the function:

$$\begin{aligned} 1000 \ln(\beta(V, T)) = & (A_1 + A_2V^{-1}) T^{-6} \\ & + (B_1 + B_2V^{-1} + B_3V^{-2}) T^{-4} \\ & + (C_1 + C_2V^{-1} + C_3V^{-2}) T^{-2}, \end{aligned} \quad (4)$$

with values of the eight coefficients given in Table 2.

X		Fo	Per	Bdm
F_0	X_0 (eV)	-7.87×10^3	-1.99×10^3	-5.88×10^3
	X_1 (eV/K)	1.09×10^{-3}	4.00×10^{-4}	9.78×10^{-4}
	X_2 (eV/K ²)	-1.04×10^{-5}	-3.17×10^{-6}	-7.17×10^{-6}
	X_3 (eV/K ³)	3.38×10^{-9}	1.06×10^{-9}	2.27×10^{-9}
	X_4 (eV/K ⁴)	-6.92×10^{-13}	-2.21×10^{-13}	-4.55×10^{-13}
	X_5 (eV/K ⁵)	5.80×10^{-17}	1.88×10^{-17}	3.78×10^{-17}
V_0	X_0 (Å ³)	3.03×10^2	77.9	1.70×10^2
	X_1 (Å ³ /K)	3.03×10^{-3}	6.86×10^{-4}	8.78×10^{-4}
	X_2 (Å ³ /K ²)	1.07×10^{-5}	3.29×10^{-6}	5.94×10^{-6}
	X_3 (Å ³ /K ³)	-4.87×10^{-9}	-1.55×10^{-9}	-2.86×10^{-9}
	X_4 (Å ³ /K ⁴)	1.23×10^{-12}	3.99×10^{-13}	7.36×10^{-13}
	X_5 (Å ³ /K ⁵)	-1.01×10^{-16}	-3.46×10^{-17}	-6.77×10^{-17}
K_0	X_0 (GPa)	1.19×10^2	1.48×10^2	2.27×10^2
	X_1 (GPa/K)	-1.02×10^{-2}	-1.08×10^{-2}	-1.26×10^{-2}
	X_2 (GPa/K ²)	-1.23×10^{-5}	-1.84×10^{-5}	-2.48×10^{-5}
	X_3 (GPa/K ³)	6.81×10^{-9}	1.03×10^{-8}	1.39×10^{-8}
	X_4 (GPa/K ⁴)	-1.78×10^{-12}	-2.68×10^{-12}	-3.62×10^{-12}
	X_5 (GPa/K ⁵)	1.74×10^{-16}	2.61×10^{-16}	3.52×10^{-16}
K'_0	X_0	4.07	4.20	3.96
	X_1 (K ⁻¹)	1.32×10^{-4}	1.15×10^{-4}	1.23×10^{-4}
	X_2 (K ⁻²)	-6.59×10^{-9}	2.00×10^{-8}	-3.98×10^{-9}
	X_3 (K ⁻³)	1.10×10^{-11}	-5.86×10^{-12}	1.96×10^{-14}
	X_4 (K ⁻⁴)	-2.73×10^{-15}	1.53×10^{-15}	8.12×10^{-16}
	X_5 (K ⁻⁵)	3.79×10^{-19}	-4.84×10^{-20}	-1.01×10^{-19}

Table 1: Polynomial coefficients of Equation 2 used to parametrise the temperature dependence of the isothermal third-order Birch-Murnaghan equation of state for each phase.

	Fo	Per	Bdm
A_1 (K ⁶)	-8.3811×10^{15}	-6.3595×10^{15}	-6.9939×10^{15}
A_2 (K ⁶ Å ³)	2.4239×10^{18}	4.7423×10^{17}	1.1706×10^{18}
B_1 (K ⁴)	-2.3070×10^{11}	-2.8718×10^{11}	-3.4351×10^{11}
B_2 (K ⁴ Å ³)	1.6240×10^{14}	4.8439×10^{13}	1.2732×10^{14}
B_3 (K ⁴ Å ⁶)	-2.9121×10^{16}	-2.1005×10^{15}	-1.2127×10^{16}
C_1 (K ²)	1.5128×10^6	2.8116×10^6	4.2687×10^6
C_2 (K ² Å ³)	-7.1553×10^8	-6.0676×10^8	-1.9792×10^9
C_3 (K ² Å ⁶)	4.4884×10^{11}	4.4657×10^{10}	2.7596×10^{11}

Table 2: Coefficients of Equation 4, used to find the reduced partition functions at chosen temperatures and cell volumes.

2 Parametrisation of magnesium fractionation in silicate liquid as a function of depth

As described in the main text, we parametrise the reduced partition function in the melt by fitting an ionic model to a range of results from hypothetical oxides in terms of bond length and coordination number as shown in Figure 4. In this approach, the reduced partition function is given by Equation 8 in the main text with the effective force constant given by Equation 7. We fix the parameter n at 12, set $z_2 = -z_1$, and we find the best fit when:

$$z_1 = (2.32716768 - 0.93910997r_0 + 0.06109785n_c) \times 2.0, \quad (5)$$

where the coordination number, n_c , and bond length r_0 , vary with hypothetical oxide and applied pressure. We assume the same parametrisation can be applied to the melt structure of [de Koker et al. \(2009\)](#) and presented in their Figure 7. We note that temperature has limited impact on coordination number and bond length and we neglect the effect of temperature on these aspects of the melt structure. We describe the evolution of bond length (in Å) with pressure (in GPa) according to the polynomial:

$$r_0 = 1.9613P - 0.00165P^2 + 0.0000019P^3 \quad (6)$$

and describe the evolution of coordination number with pressure using interpolating splines given the data points in Table 3. This parametrisation allows us to estimate the reduced partition function for melt as a function of pressure and temperature (which is included via Equation 8 of the main text). The effect of pressure on coordination number, bond length and reduced partition function of the melt is illustrated in Figure 7 of the main text.

The approaches outlined above allow the calculation of β at any chosen pressure and temperature for Per, Bdm, Fo and melt and from this we can calculate the expected isotopic fractionation using Equation 1 in the main text. This approach is used to

P (GPa)	n_c	P (GPa)	n_c
0.1	4.93	34.3	7.25
2.5	5.40	72.1	7.62
7.2	6.00	159.4	7.85
16.3	6.70		

Table 3: Mg coordination number in melt at selected pressures from [de Koker et al. \(2009\)](#).

construct Figures 6 and 9, and Table 6 in the main text. We provide an expanded version of Table 6 below (Table 4) and make the code used to perform these calculations available (see [Walker, 2025](#)).

Depth (km)	Pressure (GPa)	Temperature (K)	1000 ln(β)			
			Fo	Bdm	Per	melt
14.1	0.3	1953	0.486	0.459	0.489	0.587
98.5	2.9	2053	0.477	0.431	0.466	0.689
182.9	5.7	2154	0.467	0.406	0.446	0.756
267.3	8.6	2255	0.458	0.385	0.429	0.789
351.8	12	2354	0.449	0.366	0.413	0.797
436.2	15	2455	0.440	0.350	0.399	0.788
520.6	18	2557	0.431	0.336	0.386	0.773
605.0	21	2658	0.423	0.323	0.375	0.756
689.4	25	2761	0.415	0.311	0.364	0.736
773.9	29	2866	0.407	0.301	0.354	0.713
858.3	32	2968	0.399	0.292	0.345	0.690
942.7	36	3069	0.392	0.283	0.337	0.668
1027.1	40	3167	0.385	0.276	0.330	0.646
1111.6	44	3264	0.379	0.270	0.323	0.626
1196.0	48	3360	0.373	0.264	0.317	0.607
1280.4	52	3454	0.367	0.259	0.311	0.591
1364.8	56	3546	0.362	0.254	0.305	0.575
1449.2	60	3637	0.356	0.249	0.300	0.561
1533.7	64	3727	0.350	0.245	0.295	0.547
1618.1	68	3815	0.345	0.241	0.289	0.535
1702.5	72	3903	0.339	0.237	0.284	0.523
1786.9	76	3989	0.333	0.233	0.278	0.512
1871.4	81	4075	0.326	0.228	0.272	0.502
1955.8	85	4160	0.319	0.224	0.265	0.493
2040.2	89	4244	0.310	0.220	0.258	0.483
2124.6	93	4327	0.302	0.215	0.249	0.475
2209.0	98	4410	0.292	0.210	0.240	0.467
2293.5	102	4492	0.281	0.204	0.230	0.459
2377.9	107	4574	0.269	0.198	0.220	0.452
2462.3	111	4656	0.256	0.192	0.208	0.445
2546.7	116	4737	0.242	0.185	0.196	0.438
2631.2	121	4819	0.228	0.178	0.184	0.432
2715.6	125	4900	0.213	0.171	0.171	0.426

Table 4: Additional fractionation factors along a chondritic liquidus. Solids from DFPT with thermal expansion, liquid from an ionic model pinned to the empirical measurement at ambient pressure. See Table 4 of the main text.

References

- D. Andraut, N. Bolfan-Casanova, G. Lo Nigro, and M. A. Bouhifd. Solidus and liquidus profiles of chondritic mantle: Implication for melting of the earth across its history. *Earth and Planetary Science Letters*, 304:251 – 259, 2011. doi: 10.1016/j.epsl.2011.02.006.
- N. P. de Koker, L. Stixrude, and B. B. Karki. Thermodynamics, structure, dynamics, and freezing of Mg_2SiO_4 liquid at high pressure. *Geochimica et Cosmochimica Acta*, 72:1427 – 1441, 2009.
- P. Virtanen, R. Gommers, T. E. Oliphant, M. Haberland, T. Reddy, D. Cournapeau, E. Burovski, P. Peterson, W. Weckesser, J. Bright, S. J. van der Walt, M. Brett, J. Wilson, K. J. Millman, N. Mayorov, A. R. J. Nelson, E. Jones, R. Kern, E. Larson, C. J. Carey, Í. Polat, Y. Feng, E. W. Moore, J. VanderPlas, D. Laxalde, J. Perktold, R. Cimrman, I. Henriksen, E. A. Quintero, C. R. Harris, A. M. Archibald, A. H. Ribeiro, F. Pedregosa, P. van Mulbregt, and SciPy 1.0 Contributors. SciPy 1.0: Fundamental Algorithms for Scientific Computing in Python. *Nature Methods*, 17:261–272, 2020. doi: 10.1038/s41592-019-0686-2.
- A. Walker. andreww/isofrac: Version 0.1.0. Zenodo, 2025. URL <https://doi.org/10.5281/zenodo.16744739>.